Dynamics of suspended sediment transport

A Direct Numerical Simulation study

Shin, H. H.; Portela, L. M.; Schaerer, C. E.; Mangiavacchi, N.

DOI
10.1016/j.ijmultiphaseflow.2022.104165

Publication date
2022

Document Version
Final published version

Published in
International Journal of Multiphase Flow

Citation (APA)
Shin, H. H., Portela, L. M., Schaerer, C. E., & Mangiavacchi, N. (2022). Dynamics of suspended sediment transport: A Direct Numerical Simulation study. *International Journal of Multiphase Flow*, *155*, Article 104165. https://doi.org/10.1016/j.ijmultiphaseflow.2022.104165

International Journal of Multiphase Flow 155 (2022) 104165

Contents lists available at ScienceDirect

International Journal of Multiphase Flow

journal homepage: www.elsevier.com/locate/ijmulflow

Dynamics of suspended sediment transport: A Direct Numerical Simulation study

H.H. Shin [a,b,c,*], L.M. Portela [b], C.E. Schaerer [a], N. Mangiavacchi [c]

[a] Núcleo de Investigación y Desarrollo Tecnológico, Universidad Nacional de Asunción, Campus de la UNA, Villa Universitaria, San Lorenzo, C.C. 2111, Central, Paraguay

[b] Department of Chemical Engineering, Delft University of Technology, Van der Maasweg 9, 2629 HZ, Delft, The Netherlands

[c] Department of Mechanical Engineering, Universidade do Estado do Rio de Janeiro, Rua Fonseca Teles 121, São Cristóvão, Rio de Janeiro, 20940-903 RJ, Brazil

ARTICLE INFO

Keywords:
Point-particle Direct Numerical Simulation
One-way coupling
Resuspension
Virtual wall
Suspended sediment
Fluid–particle interaction

ABSTRACT

The dynamics of suspended sediment transport in horizontal open channel flow is analysed using point-particle one-way coupling Direct Numerical Simulations (DNS), with a virtual wall as a simple particle resuspension model. In sediment transport, the bed-load is dominated by the inter-particle interactions, but the suspended sediments are transported essentially in a one-way coupling situation. The validity of one-way coupling DNS with point-particle approach for the transport of suspended sediment is analysed, by comparing the simulations with existing well-designed experiments performed under very similar conditions. The range of the relevant non-dimensional parameters of the simulations is roughly the same as in actual sediment transport, except for the flow Reynolds number. Good agreement is observed between the simulations and the experiments; furthermore, the simulation results of the motion of the suspended sediment are insensitive to the position of the virtual wall, provided this wall is placed in a region where the fluid velocity fluctuation in the wall-normal direction is comparable to the particle settling velocity. Using the simulation results, the interplay between the different fluid–particle interaction forces is analysed, with and without gravity. In the absence of gravity, the dynamics is dominated by the balance between the stress-gradient force and the turbophoretic effects; as the particle-to-fluid density ratio for the sediment particles is on the order of one, the situation is quite different when compared to the dynamics with a density ratio on the order of 1000. When gravity is included, the dynamics is dominated by the interplay between the drag and gravitational forces, and they balance each other. Both with and without gravity, the lift and added-mass forces have only secondary effects and do not play an important role.

1. Introduction

Sediment transport is a process involved in many natural and man-made applications. The transport of sand-like sediment in turbulent water flow has been widely studied due to its importance in the human development and survival, and also for the environmental sustainability (Chien and Zhaohui, 1999; García, 2008).

Complex physics are involved in the sediment transport in open channel flow. Close to the channel bed, highly concentrated sediment particles are transported by the damped but still turbulent fluid flow, while they strongly interact with the channel bed and also between them by collision. Away from the channel bed, the sediment particles with diluted concentration are transported by the turbulent flow. Thus, a more computationally efficient analysis is possible by splitting the transport mechanisms into bed-load transport and suspended-load transport (Chanson, 2004; Wu, 2007; García, 2008). Despite the intensive studies done in both transport processes, there is a lack of knowledge in the modelling and simulation of the phenomena (Ancey, 2020a,b; Rodi, 2017; Sotiropoulos, 2015, 2019).

In this work, the dynamics of suspended sediment transport is studied using the point-particle one-way coupling Direct Numerical Simulation (DNS), focusing on the different mechanisms and forces involved. This model/approach has been playing an important role as a research tool for an improved understanding of the physic involved, and therefore to provide better support for the development of engineering models, like two-fluid models based on Reynolds-Averaged equations (Portela and Oliemans, 2006).

* Correspondence to: Facultad Politécnica, Universidad Nacional de Asunción, Campus de la UNA, Villa Universitaria, San Lorenzo, C.C. 2111, Central, Paraguay.

E-mail addresses: hshin@pol.una.py (H.H. Shin), l.portela@tudelft.nl (L.M. Portela), cschaer@pol.una.py (C.E. Schaerer), norberto.mangiavacchi@eng.uerj.br (N. Mangiavacchi).

https://doi.org/10.1016/j.ijmultiphaseflow.2022.104165
Received 4 March 2022; Received in revised form 24 May 2022; Accepted 10 June 2022
Available online 20 June 2022

Thus, in applications of gas–solid and gas–liquid flows, the point-particle DNS has been extensively used (Portela and Oliemans (2006), Marchioli et al. (2008), among many others), but this approach was not exploited enough in applications of sediment transport. The main difference between the sediment transport and gas–solid/liquid applications is the particle-to-fluid density ratios. This ratio in gas–solid/liquid flows is on the order of $\mathcal{O}(1{,}000)$, which allows to neglect some force terms in the fluid–particle interactions, while the most relevant interaction force is usually the drag force. Contrarily, the density ratio of sediment particles to the fluid is slightly larger than one. This brings into play other fluid–particle interaction forces in addition to the drag force, such as the stress-gradient and the added mass forces. In this work, the point-particle one-way coupling DNS is used in order to evaluate the interplay between several fluid–particle interaction forces and their relative importance, in the absence of gravitational, and as well as in the presence of the gravitational force in the wall-normal direction.

When the gravitational force acts on the particles in wall-normal direction, the inter-particle interactions become dominant in the bed region due to the high particle-concentration. However, once the particles are resuspended by the interactions of fluid–particle and inter-particle, the particle-concentration restricted to the suspended sediment is much lower, thus one-way coupling might be a good assumption for the suspended sediment. On the other hand, the strict requirement of point-particle is not formally satisfied because the sizes of the sediment particles are not always small enough compared to the smallest turbulence length-scales. Thus, a question to be explored in this article is whether the DNS with the assumptions of point-particle and one-way coupling, and additionally with a pragmatic simple resuspension model (a kind of wall-function for the particles) is enough for the analysis of the suspended sediment transport based on the decoupled behaviour of sediment transport mechanism. The approach is validated by comparing with an existing experiment which has been designed in order to performe one-to-one comparison with DNS (Breugem, 2012).

As a simple resuspension model, a virtual wall, which consists of a horizontal plane located at a short distance above the bottom wall for the bouncing of the particles, is used. Although the virtual wall has been already used by Cargnelutti and Portela (2007) and Soldati and Marchioli (2012), the effects of the positions of the virtual wall on the dynamics of the suspended sediments have not been extensively addressed. Therefore, as another contribution of this work, a sensitivity analysis of the position of the virtual wall, together with different statistics of suspended particle motions are presented, and compared with the experimental results.

The work is organised as follows: first, the formulation of the point-particle DNS used in this work, together with the theoretical background of the virtual wall model and the momentum balance of the particle phase are presented in Section 2. In Section 3, the numerical method with the parameter sets used in the simulations are given; and the details of the numerical experiments together with the selection of the position of the virtual wall are presented. The results of the simulations and the discussions are given in Section 4, and finally, Section 5 gives the final remarks.

2. Modelling equations

The equations used in the point-particle one-way coupling DNS for the simulation of particle laden flow are presented in Section 2.1. Then, the resuspension mechanism of the sediment particles and a theoretical background in which the virtual wall might work as a particle resuspension model are given in Section 2.2. Finally, Section 2.3 shows the development of the average-momentum balance equations for the particles. Each term which arises in these equations can be computed using the results of point-particle one-way coupling DNS, and therefore, analysis of the contribution of each term in the whole particle dynamics can be made.

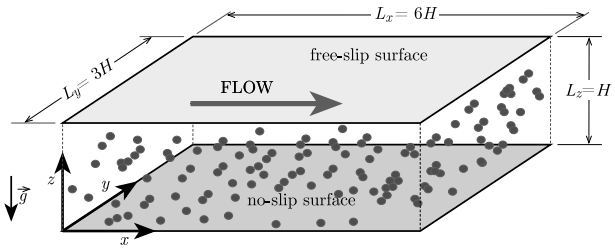

Fig. 1. Open-channel domain.

2.1. Point-particle one-way coupling DNS

In the sediment transport, there are two phases: the water flow described by the continuous phase and the sediment particles by the dispersed phase. The continuous phase is modelled as an incompressible flow of a Newtonian fluid, described by the continuity and Navier–Stokes equations. In this work, we consider suspended sediment transport in a dilute situation. Therefore, one-way coupling is assumed, where the effects of the particles on the fluid flow and particle collisions are neglected, so the fluid flow equations are solved without including any additional terms. Three-dimensional rectangular coordinate system with x in flow streamwise direction, y in spanwise direction, and z in wall-normal direction is considered (Fig. 1).

The fluid flow equations are given by:

$$\nabla \cdot \vec{u}_f = 0, \tag{1}$$

$$\frac{D\vec{u}_f}{Dt} = -\frac{\nabla p}{\rho_f} + \nu \nabla^2 \vec{u}_f + \vec{g}, \tag{2}$$

where $\vec{u}_f$ is the fluid velocity with the components u_f, v_f and w_f; p the fluid pressure, ρ_f the fluid density and ν is the fluid kinematic viscosity, given by $\nu = \mu/\rho_f$, where μ is fluid dynamic viscosity, and $\vec{g}$ is the acceleration of gravity. The operator D/Dt is the material derivative, which provides the time derivative following a fluid particle, *i.e.*, $D/Dt = \partial/\partial t + \vec{u}_f \cdot \nabla$. The flow Reynolds number is defined as $\mathrm{Re}_\tau = u_\tau H/\nu$, where u_τ is the friction velocity and H is the channel height. The friction velocity is related in terms of wall-shear stress τ_w given by $\tau_w = \rho_f u_\tau^2$.

Maxey and Riley (1983) presented the equation of motion for a small rigid sphere immersed in non-uniform and unsteady flows. From that equation, the Basset history-force is customarily neglected, even for sediment transport simulations (Cargnelutti and Portela, 2007; Vinkovic et al., 2011; Soldati and Marchioli, 2012); and the lift force is included. Thus, the equation for particle motion used in this work becomes:

$$\rho_p \mathcal{V}_p \frac{d\vec{u}_p}{dt} = 3\pi\mu d_p(\vec{u}_f - \vec{u}_p) + \rho_p \mathcal{V}_p \vec{g} + \frac{1}{2}\rho_f \mathcal{V}_p \left(\frac{D\vec{u}_f}{Dt} - \frac{d\vec{u}_p}{dt} \right) + \mathcal{V}_p \left(\nabla \cdot \vec{\tau} \right) + \vec{F}_L, \tag{3}$$

where $\vec{u}_p$ is the particle velocity with the components u_p, v_p and w_p; the fluid velocity $\vec{u}_f$ is evaluated at the position of the centre of the particle, ρ_p the particle density, d_p the particle diameter, $\vec{\tau}$ the surrounding fluid stress tensor, $\mathcal{V}_p = \pi d_p^3/6$ the particle volume and $\vec{F}_L$ is the lift force. The particle Reynolds number is defined as $\mathrm{Re}_p = u_\tau d_p/\nu$, but it can also be defined based on particle velocity relative to the local fluid velocity as $\mathrm{Re}_r = |\vec{u}_f - \vec{u}_p|\, d_p/\nu$. The forces which appears in Eq. (3) are: (i) the drag force modelled as Stokes drag which is valid in the limit of small particle Reynolds number based on relative velocity, (ii) the gravitational force, (iii) the added-mass force with the coefficient 1/2, (iv) the surrounding fluid-stress, and (v) the lift force.

The lift force included in this work is composed by: (i) the "optimum lift force" model formulated by Wang et al. (1997) which is a compilation of different models available in the literature for the lift force acting on a particle in a shear-flow bounded by a wall; and (ii) the lift force proposed by Krishnan and Leighton (1995) for particles touching the wall. When the particle is away from the wall, the "optimum lift force" model formulated by Wang et al. (1997) is applied using the expression:

$$F_L = -\frac{9}{\pi}\mu a^2 U_s \,\mathrm{sign}(G)\left[\frac{|G|}{\nu}\right]^{1/2} J, \tag{4}$$

where U_s is the slip-velocity, which is the difference between the particle and fluid streamwise velocities (parallel to the wall), G is the velocity-shear, which is the wall-normal gradient of the fluid streamwise velocity at the particle position, $a = d_p/2$ is the particle radius, and J is a function that takes into account both contributions: (i) the shear in an unbounded flow, and (ii) the presence of the wall. For the expressions and/or values of J together with the conditions in which they are valid, the following works Wang et al. (1997), McLaughlin (1991, 1993) and Arcen et al. (2006) can be referred. Wang et al. (1997) also included the expression:

$$F_L = \rho_f a U_s I_{cm}, \tag{5}$$

in order to consider the cases when the space between the wall and the particle are comparable to the particle radius. This expression was initially given by Cherukat and McLaughlin (1994), who presented the values of I_{cm} as a best-fitting equation. Also, the expression

$$F_L = 9.257\rho_f G^2 a^4 + 1.755\rho_f U_s^2 a^2 - 9.044\rho_f G U_s a^3, \tag{6}$$

proposed by Krishnan and Leighton (1995) is included into the lift force, when the particle is touching the wall. The lift force shown in the Eqs. (4)–(6) corresponds to the component in the wall-normal direction, whereas the other components are zero.

The acceleration of the surrounding fluid in terms of fluid stress is given by:

$$\frac{D\vec{u}_f}{Dt} = \frac{1}{\rho_f}\left(\nabla\cdot\vec{\tau}\right) + \vec{g}. \tag{7}$$

By including the above equation into Eq. (3), we can express the equation of the particle motion as:

$$\frac{d\vec{u}_p}{dt} = \frac{1}{t_a}(\vec{u}_f - \vec{u}_p) + \frac{\beta-1}{\beta+{}^1/_2}\vec{g} + \frac{{}^3/_2}{\beta+{}^1/_2}\frac{D\vec{u}_f}{Dt} + \frac{\beta}{\beta+{}^1/_2}\vec{f}_L, \tag{8}$$

where, $\beta = \rho_p/\rho_f$ is the particle-to-fluid density ratio, $t_a = [(\beta+1/2)/\beta]t_p$ is a modified particle relaxation time, which is related to the particle relaxation time, $t_p = \beta d_p^2/18\nu$, and $\vec{f}_L = \vec{F}_L/\rho_p\mathcal{V}_p$ is the lift force per unit of mass of a particle. The factor $[(\beta+1/2)/\beta]$ in the particle relaxation time is due to the presence of added-mass force in the particle equation, which gives a contribution of additional inertia to the particle movement.

The dimensionless form of Eq. (8) for the particle motion can be obtained considering the friction velocity u_τ, and the viscous length-scale $\delta_\nu = \nu/u_\tau$, as follows:

$$\frac{d\vec{u}_p^+}{dt^+} = \frac{1}{\mathrm{St}_a}(\vec{u}_f^+ - \vec{u}_p^+) + \frac{1}{\mathrm{Fr}_a^2}\frac{\vec{g}}{g} + \frac{{}^3/_2}{\beta+{}^1/_2}\frac{D\vec{u}_f^+}{Dt^+} + \frac{\beta}{\beta+{}^1/_2}\vec{f}_L^+, \tag{9}$$

where the variables with superscript, $\cdot^+$, correspond to the non-dimensional forms based on viscous scales, or wall-unit, given by u_τ and δ_ν, and g is the magnitude of the gravity acceleration. The Stokes number is defined as a ratio between particle relaxation time and fluid viscous timescale: $\mathrm{St} = t_p/t_\nu$, thus the modified Stokes number is expressed as $\mathrm{St}_a = t_a/t_\nu$; the viscous timescale is given by $t_\nu = \delta_\nu/u_\tau$. Both Stokes numbers differ in a factor associated to the particle-to-fluid density, as: $\mathrm{St}_a = [(\beta+1/2)/\beta]\,\mathrm{St}$.

The particle Froude number, Fr, associates the fluid inertia with the gravitational effects on the particle, and the modified particle Froude number, Fr_a, is defined as:

$$\frac{1}{\mathrm{Fr}_a^2} = \frac{w_s^+}{\mathrm{St}_a}. \tag{10}$$

In this equation, $w_s = g_r t_p$ is the magnitude of the particle settling velocity in a stagnant medium, where the reduced gravity is defined as $g_r = g(\beta-1)/\beta$. Similarly to the Stokes number, the modified particle Froude number differs from the particle Froude number by a factor associated to the particle-to-fluid density, *i.e.*: $\mathrm{Fr}_a^2 = [(\beta+1/2)/\beta]\,\mathrm{Fr}^2$, and the particle Froude number is defined as $\mathrm{Fr}^2 = \mathrm{St}/w_s^+$.

From Eq. (9), it can be noticed that the dynamics of the particle motion depends on three non-dimensional parameters: (i) the (modified) Stokes number associated to the drag force, (ii) the (modified) particle Froude number which emerges with the presence of gravitational force, and (iii) the particle-to-fluid density ratio which affects in the importance of the fluid-acceleration term and the lift force. The fluid-acceleration term is linked to the fluid stress-gradient and added-mass forces.

In the absence of the gravitational force, the relevant parameters are the Stokes number and the particle-to-fluid density ratio. Particularly, for gas–solid/liquid flows, the modified Stokes number becomes very similar to the Stokes number, and the term which contains the fluid-acceleration vanishes due to the large particle-to-fluid density ratio. Furthermore, besides the coefficient of the lift force (in Eq. (9)) is on the order of $\mathcal{O}(1)$, the effects of this force on the statistics of the particle distribution are not negligible but not dominant (Arcen et al., 2006). Thus, the term associated to the drag force usually dominates the dynamics of the particle in gas–solid/liquid flows. On the other hand, in sediment transport, the particle-to-fluid density ratio is on the order of $\mathcal{O}(1)$, so the term which contains the fluid-acceleration, *i.e.*, the stress-gradient and added-mass forces, might become important, as well as the drag force. As the coefficient of the lift force is also on the order of $\mathcal{O}(1)$ independent of the particle-to-fluid density ratio, it is not well known whether the lift force might be important in the motion of sediment particles in the absence of gravitational force.

The particle Froude number emerges when the wall-normal gravitational force acts on the particles. In gas–solid/liquid flows, the drag force and the gravitational force dominate the dynamics of the particle. On the other hand, in addition to these forces, in suspended sediment transport the fluid-acceleration term might be important due to the order of $\mathcal{O}(1)$ of particle-to-fluid density ratio; and the effect of the lift force might be different compared to the gas–solid/liquid flows. As the gravitational force is introduced into the particle equation, whether the particles are resuspended or not is determined by the particle Froude number. From Eq. (10), it can be noticed that the particle Froude number is associated to the particle settling velocity normalised by the friction velocity and the Stokes number. Because the gravitational force is only present in the wall-normal direction, it is possible to define the particle Froude number in terms of representative fluctuation of wall-normal fluid velocity, which has the same order of magnitude than the friction velocity. Also, as the Stokes number for the sediment particles is on the order of $\mathcal{O}(1)$, the ratio of particle settling velocity to the wall-normal fluid velocity fluctuation will determine whether the sediment particles are resuspended or not.

The next subsection gives the description of the resuspension model used in this work. Then, the average of the equation of particle motion is presented in Section 2.3, and the evaluation of the importance of each fluid–particle interaction force is shown in Section 4.

2.2. A resuspension model: virtual wall

The entrainment of sediment particles into suspension from the channel bed has been largely studied in the last century, but there is still lack of knowledge to understand the whole phenomena (Dey

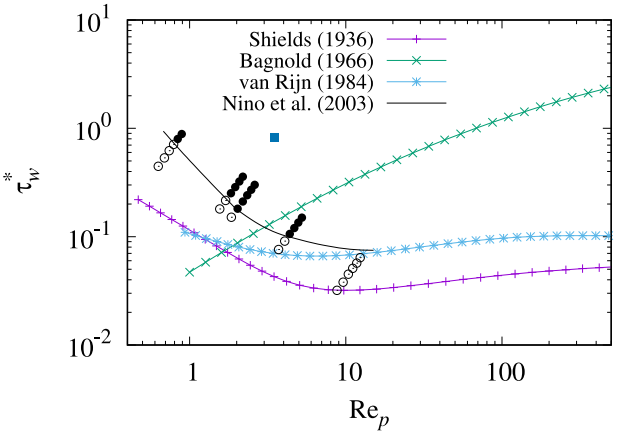

Fig. 2. Thresholds curves: The curve of Shields (1936) is a fit given by Brownlie (1981) for initiation of sediment bed movement; the curve of van Rijn (1984) is a fit given by van Rijn (2020) for particle suspension; the curve of Niño et al. (2003) is a threshold curve (drawn by hand) which separates the suspended particles (•) and no-suspension (∘); the curve of Bagnold (1966) is a theoretical curve for the particle suspension. The blue square symbol at $\left(\mathrm{Re}_p = 3.47, \tau_w^* = 0.82\right)$ corresponds to the parameters used in this work.

and Ali, 2019). A complex combination of instantaneous fluid turbulence around the particle, the properties of the sediment particle and the sediment bed characteristics influence strongly in the entrainment phenomena (Coleman and Nikora, 2008). An extensive review of different mechanism of sediment entrainment is beyond the aim of this work. Instead, we are interested in studying the dynamics of suspended sediment transport, and we are going to explore whether a very simple resuspension model, using a virtual wall, is reasonable for the simulation of suspended sediment transport; and then, we are going to analyse the sensitivity of this model.

There are sets of particle parameters associated to the flow conditions, in which the particles deposited on the bottom wall are re-entrained into suspension. Normally, these sets are presented as a threshold of bed shear stress in terms of particle diameter (Niño et al., 2003; Dey and Ali, 2019). The bed shear stress in dimensionless form τ_w^*, known as Shields' stress, is defined as:

$$\tau_w^* = \frac{u_\tau^2}{g(\beta - 1)d_p}, \tag{11}$$

and the dimiensionless particle diameter is equivalent to the particle Reynolds number Re_p.

Fig. 2 shows some threshold curves. Shields (1936) presented a critical bed shear stress for the initiation of particle movement on the bed from experimental results (a fit proposed by Brownlie (1981) is shown). Note that the Shields threshold is for the particle movement, therefore larger bed shear stress compared to this threshold is required for the particle suspension. A threshold for the initiation of particle suspension was first determined by van Rijn (1984) (a fit given by van Rijn (2020)) from experimental observation of particles which are lifted by upward fluid-turbulence and maintained suspended for a distance about 100 particle diameters. With a similar criterion, Niño et al. (2003) performed experimental observation and classified the parameter-sets of the particles and flows, as "suspension" if the particles lifted by the fluid turbulence are maintained suspended for distance larger than 100 particle diameters, or as "no suspension" if not. Fig. 2 also shows a curve drawn by hand, similar to the one drawn by Niño et al. (2003), which separates the suspended particles from those not suspended.

A theoretical condition for the particle resuspension was given by Bagnold (1966), based on the idea that the root-mean-square (rms) of vertical upward components of the fluid velocity fluctuations ($w'_{f_{up}}$), which has its maximum on the same order of magnitude than the friction velocity (u_τ), should be greater than or equal to the magnitude of particle settling velocity (w_s). However, this maximum value of the rms fluid vertical fluctuation occurs in the log-law region (at about $z^+ \approx 60$ for $\mathrm{Re}_\tau = 500$); it decreases as the wall is approached, and it is highly damped in the viscous sub-layer, reaching zero on the wall (see Fig. 4). This means that, for a small isolated particles submerged in the viscous sub-layer, the drag force due to the fluctuations of the wall-normal fluid velocity would not be sufficient to overcome the gravitational force. In this particular situation, the lift force would have an important role, giving an upward impulse that could contribute to the resuspension of an isolated particle (Vollmer and Kleinhans, 2007).

As the particles accumulate near the bottom wall due to the gravitational effects, the highly dense flow is observed, and thus, complex fluid–particle, wall-particle and inter-particle interactions determine the particle resuspension mechanism. This complex resuspension mechanism cannot be modelled by one-way coupling assumption. However, above this dense flow region, there is a small transition region, and further away, the flow with sediment transport is very dilute, and thus it is essentially one-way coupling. Therefore, in statistically steady-state, when a particle approaches the wall, it enters into the region where the particle-concentration is moderate to high, and this particle is re-entrained into suspension after the complex interactions present in this region. As the sediment particles have small particle relaxation-time, the re-entrained particles can accommodate quickly to the local fluid turbulence. Thus, it might be possible to avoid the representation of this complex resuspension mechanism by using simply a virtual wall located a small distance from the bottom wall, where the particles approaching the wall are bounced and re-entrained into suspension. The virtual wall consists of a horizontal plane parallel to the bottom wall and separated from this a small distance for the effective bouncing of the particles.

Actually, the point-particle one-way coupling simulations are not able to represent the complex phenomena near the bed-region, regardless of the inclusion of any fluid–particle interaction force model. Thus, the virtual wall model would be effective to bring the particles to a distance from the bottom where the fluctuations of the wall-normal fluid velocity become higher, so the drag force would balance the gravitational force maintaining suspended the particles, thus enforcing the resuspension criterion for the particle.

In this context, following the idea of Bagnold (1966), a local particle Froude number can be defined based on the rms of local wall-normal fluctuating fluid velocity instead of the friction velocity. Thus, for the rms of local wall-normal fluctuating fluid velocity expressed as:

$$w'_{f,\mathrm{rms}}(z) = \sqrt{\left\langle w'_f(z) w'_f(z) \right\rangle_f}, \tag{12}$$

with the operator $\langle\cdot\rangle_f$ denoting the ensemble average, and the subscript $\cdot_f$ indicating that the computation of the averaging is taken over the fluid volume, it can be defined the local particle Froude number as:

$$\frac{1}{\mathrm{Fr}_l^2(z)} = \frac{1}{\mathrm{St}_a} \frac{w_s}{w'_{f,\mathrm{rms}}(z)}. \tag{13}$$

The fluctuating part of the fluid velocity is obtained subtracting the average fluid velocity $W_f = \langle w_f \rangle_f$ from the instantaneous fluid velocity in the corresponding component w_f, and thus: $w'_f = w_f - W_f$. As the fluctuations of fluid velocity increase as farther away from the wall, so do the local particle Froude number. Once the particles are placed in a region where this local Froude number is on the order of $\mathcal{O}(1)$ (or larger), the drag force associated to the fluctuating fluid velocity would be sufficient to balance the gravitational force. It can be noted that this local particle Froude number is essentially the ratio between the particle settling velocity to the local rms of wall-normal fluctuating

fluid velocity. Thus, the position of the virtual wall is selected based on this ratio. Then, the sensitivity analysis of the positions of the virtual wall on the dynamics of the suspended sediment particles are performed.

2.3. Average particle momentum balance equations

The ensemble average of the particle momentum equation can be expressed as (Drew, 1983; Enwald et al., 1996):

$$\frac{\partial}{\partial t}\left(\alpha_p\rho_p\left\langle\vec{u}_p\right\rangle_p\right)+\nabla\cdot\left(\alpha_p\rho_p\left\langle\vec{u}_p\vec{u}_p\right\rangle_p\right)$$
$$=\nabla\cdot\left(\alpha_p\left\langle\vec{\bar{\tau}}_p\right\rangle_p\right)+\alpha_p\rho_p\vec{g}-\left\langle\vec{\bar{\tau}}\cdot\nabla\chi_p\right\rangle_p, \tag{14}$$

where, α_p is the particle concentration and $\langle\cdot\rangle_p$ represents the ensemble average operator, where the subscript p indicates that the computation of the averaging is taken over the particles. The ensemble average of the particle velocity is $\vec{U}_p = \left\langle\vec{u}_p\right\rangle_p$. Thus, the average of the convective term $\nabla\cdot(\alpha_p\rho_p\left\langle\vec{u}_p\vec{u}_p\right\rangle_p)$ is split into an average convection $\nabla\cdot(\alpha_p\rho_p\vec{U}_p\vec{U}_p)$, and a term associated to the particle Reynolds-stress tensor $\nabla\cdot(\alpha_p\rho_p\left\langle\vec{u}'_p\vec{u}'_p\right\rangle_p)$, where the prime symbol, $\cdot'$, denotes the difference between the instantaneous and average values.

The first term in the right-hand side (rhs) of Eq. (14) is the stress in the particle phase, and it is only relevant in dense flow, when the collisions between particles are important. The second term accounts for the gravitational effects, and the last term is the force density exerted by the fluid on the particles due to the fluid–particle interaction. As the average particle momentum equations are evaluated using point-particle one-way coupling simulations, the term associated to the particle collision is neglected and the fluid–particle interaction term is split into the specific forces included in the DNS performed. The fluid–particle interaction force density is expressed using the phase indicator function χ_p, defined as $\chi_p(\vec{x}) = 1$ when there is a particle in $\vec{x}$, or 0 otherwise. By considering Stokes drag, added-mass, surrounding fluid stress, and lift force, the force density is expressed as:

$$-\left\langle\vec{\bar{\tau}}_p\cdot\nabla\chi_p\right\rangle_p=\alpha_p\left[\frac{18\mu}{d_p^2}\left\langle\vec{u}_f-\vec{u}_p\right\rangle_p+\rho_f\left\langle\frac{D\vec{u}_f}{Dt}\right\rangle_p\right.$$
$$\left.+\frac{1}{2}\rho_f\left\langle\frac{D\vec{u}_f}{Dt}-\frac{d\vec{u}_p}{dt}\right\rangle_p-\rho_f\vec{g}+\rho_p\left\langle\vec{f}_L\right\rangle_p\right]. \tag{15}$$

Thus, this expression can be replaced in Eq. (14), and it can be further reduced based on the statistically-steady fully-developed particle-laden channel-flow assumption in one-way coupling, as:

$$\left(1-\frac{1}{\beta}\right)\vec{g}+\frac{1}{t_p}\vec{U}_{rel}+\frac{1}{\beta}\left\langle\frac{D\vec{u}_f}{Dt}\right\rangle_p+\left\langle\vec{f}_L\right\rangle_p$$
$$+\frac{1}{2\beta}\left\langle\frac{D\vec{u}_f}{Dt}-\frac{D\vec{u}_p}{Dt}\right\rangle_p-\frac{1}{\alpha_p}\nabla\cdot\left(\alpha_p\left\langle\vec{u}'_p\vec{u}'_p\right\rangle_p\right)=0 \tag{16}$$

where, $\vec{U}_{rel}$ is the average relative velocity between the fluid and particle, defined as:

$$\vec{U}_{rel}=\left\langle\vec{u}_f-\vec{u}_p\right\rangle_p=\vec{U}_f+\left\langle\vec{u}'_f\right\rangle_p-\vec{U}_p, \tag{17}$$

where $\vec{U}_f$ is the average fluid velocity. The term $\left\langle\vec{u}'_f\right\rangle_p$ is the average fluid velocity fluctuation at the particle position, known as "drift velocity", which accounts for the dispersion of the particles due to the fluctuating fluid velocity (Simonin et al., 1993).

From the left to the right of Eq. (16): the first term is the combination of gravity and buoyancy or simply gravity term, the second is the Stokes drag contribution, the third is the stress-gradient, the fourth is the lift force contribution, and the fifth is the added-mass. The last term is the contribution of the particle Reynolds-stress which can be split into two terms as follows:

$$-\frac{1}{\alpha_p}\nabla\cdot\left(\alpha_p\left\langle\vec{u}'_p\vec{u}'_p\right\rangle_p\right)=-\left\langle\vec{u}'_p\vec{u}'_p\right\rangle_p\cdot(\nabla\ln\alpha_p)-\nabla\cdot\left\langle\vec{u}'_p\vec{u}'_p\right\rangle_p, \tag{18}$$

where the first term on the rhs relates to the momentum transfer due to the diffusion process or concentration gradient, *i.e.*, particles moving from high to low particle-concentration, but in this case mostly damped by the near-wall fluid turbulence; the second term relates to the effects of "turbophoresis", in which the particles migrate from high to low fluid turbulence intensities (Reeks, 1983). From Eq. (16), it can be seen that the terms containing particle Reynolds-stresses emerge in the averaging process of the momentum equation for the particles, and they contribute to the net motion of the particles.

The Eq. (18) is substituted into Eq. (16), and thus, Eq. (19) shows the momentum balance of the streamwise component and Eq. (20) gives the balance in the wall-normal direction. Both equations are presented in the dimensionless forms based on the friction velocity u_τ and the viscous length-scale δ_ν. All spanwise momentum contributions become statistically zero due to symmetry consideration. Each term in both Eqs. (19) and (20) has an under-brace with an abbreviation in order to identify the specific contribution: D is drag force contribution, SG is stress-gradient, AM is added-mass force, GB is gravitational effect, CG is the diffusion effect, TP is turbophoretic effect and L is lift force contribution (Eqs. (19) and (20) are given in Box I).

3. Numerical method

3.1. Simulation set-up

The flow is driven by a constant streamwise pressure-gradient. The motion of continuous-phase, represented by the Eqs. (1) and (2), is obtained from a standard finite-volume code based on a predictor–corrector solver on a staggered-grid, with a second-order Adams–Bashforth scheme for time-integration in the predictor-step. The pressure is obtained from the Poisson equation which is solved applying fast-Fourier transform in stream and spanwise directions, and solving the tri-diagonal matrices in wall-normal direction. The velocity field is corrected from the obtained pressure field. The time-step is determined adaptively by the Courant stability criterion. Free-slip boundary condition at the top of the channel and no-slip condition at the bottom wall are imposed; periodic-boundary conditions are used in the stream and spanwise directions (see Fig. 1).

The particles are assumed to be point-wise. The equation of particle-motion, Eq. (9), is integrated using an explicit second-order Runge–Kutta scheme, and a trilinear interpolation is employed to calculate the fluid velocity at the centre of the particle. The top and bottom walls are considered as elastic bouncing-walls (see Fig. 3(left)), which means that, when the distance of the centre of a particle to the bottom wall is lower than a particle radius, we perform the specular reflection of the particle with respect to the bottom wall. For the particles, periodic-boundary conditions are also used in stream and spanwise directions, *i.e.*, the particle leaving the computational-domain out of a periodic-boundary is reintroduced into the opposite boundary. More details of the code can be found in Portela and Oliemans (2003).

When the virtual wall is included into the simulations, this wall is a horizontal plane parallel to the bottom wall and is considered as elastic bouncing-wall for the particles (see Fig. 3(right)). This means that, when the distance of the centre of a particle to the virtual wall is lower than a particle radius, we perform the specular reflection of the particle with respect to the virtual wall.

The parameters of the flow and the particles for the present simulations are taken from the experimental setup of Breugem and Uijttewaal (2006) and Breugem (2012). In those works, the physical parameters in the experiments were carefully chosen in order to allow direct comparison with DNS. Thus, the higher flow Reynolds number was

$$\underbrace{\frac{1}{\mathrm{St}}\left(U_f^+ - U_p^+ + \left\langle u_f'^+\right\rangle_p\right)}_{\mathrm{D}} + \underbrace{\frac{1}{\beta}\frac{d\left\langle u_f'^+ w_f'^+\right\rangle_p}{dz^+}}_{\mathrm{SG}} + \underbrace{\frac{1}{2\beta}\left(\frac{d\left\langle u_f'^+ w_f'^+\right\rangle_p}{dz^+} - \frac{d\left\langle u_p'^+ w_p'^+\right\rangle_p}{dz^+}\right)}_{\mathrm{AM}} \underbrace{- \left\langle u_p'^+ w_p'^+\right\rangle_p \frac{d\ln\alpha_p}{dz^+}}_{\mathrm{CG}} \underbrace{- \frac{d\left\langle u_p'^+ w_p'^+\right\rangle_p}{dz^+}}_{\mathrm{TP}} = 0, \tag{19}$$

$$\underbrace{-\frac{1}{\mathrm{Fr}^2}}_{\mathrm{GB}} + \underbrace{\frac{1}{\mathrm{St}}\left\langle w_f'^+\right\rangle_p}_{\mathrm{D}} + \underbrace{\frac{1}{\beta}\frac{d\left\langle w_f'^+ w_f'^+\right\rangle_p}{dz^+}}_{\mathrm{SG}} + \underbrace{\frac{1}{2\beta}\left(\frac{d\left\langle w_f'^+ w_f'^+\right\rangle_p}{dz^+} - \frac{d\left\langle w_p'^+ w_p'^+\right\rangle_p}{dz^+}\right)}_{\mathrm{AM}} \underbrace{- \left\langle w_p'^+ w_p'^+\right\rangle_p \frac{d\ln\alpha_p}{dz^+}}_{\mathrm{CG}} \underbrace{- \frac{d\left\langle w_p'^+ w_p'^+\right\rangle_p}{dz^+}}_{\mathrm{TP}} + \underbrace{\left\langle f_L^+\right\rangle_p}_{\mathrm{L}} = 0. \tag{20}$$

Box I.

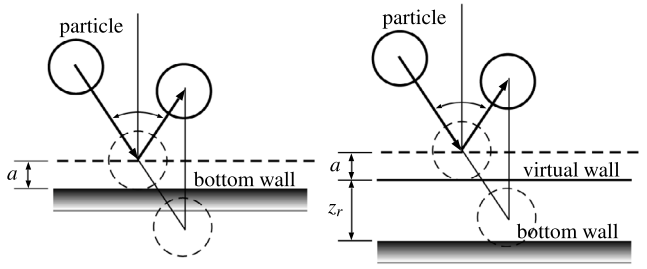

Fig. 3. The elastic bouncing wall for the particles: (left) bottom wall without virtual wall, (right) with virtual wall. a: particle radius, z_r: distance between virtual wall and bottom wall. The particles are relocated into a symmetrical position with reflective velocity.

Table 1
Simulations performed. In each simulated case, a mark "×" indicates that the corresponding force or model is included in the particle-motion. The acronyms for the forces/models are: GB: gravity (submerged weight), D: Stokes drag force, SG: stress-gradient force, AM: added-mass force, L: lift force, VW: virtual wall model.

Id	Re_τ	Forces/models on the particles					
		GB	D	SG	AM	L	VW
hRe-d	500		×	×	×		
hRe-l	500		×	×	×	×	
hRe-gl	500	×	×	×	×	×	
hRe-v1/6	500	×	×	×	×		×
lRe-d	180		×	×	×		
lRe-l	180		×	×	×	×	
lRe-gl	180	×	×	×	×	×	
lRe-v1/6	180	×	×	×	×		×

limited by affordable DNS which was about $\mathrm{Re}_\tau = 500$, with bulk Reynolds number about $\mathrm{Re}_b = 10{,}000$ which was obtained by setting the centre-line velocity to 0.2 m/s and 0.050 m for the water-depth. With the reduction of flow Reynolds number, in order to maintain the particle Froude number similar to the suspended sediment transport in the river, the reduction of particle density is inevitable (see Eq. (10)). Thus, natural sediment could not be used in the experiments. Instead, polystyrene particles with a density of $\rho_p = 1035$ kg/m^3 and mean diameter of $d_p = 347$ μm were used as pseudo-sediment. At the selected flow velocity and particles, a sufficient amount of sediment in the water column was ensured ($u_\tau/w_s \approx 5$). Although the density of the particles used in the experiments was different to the sand-like sediment, the non-dimensional parameter values were similar to those in rivers or in experiments with real sand, and Breugem (2012) had observed all the characteristics involved in the transport of suspended sediments using real sand. It is worth to mention that the experiments of Breugem and Uijttewaal (2006) and Breugem (2012) had been designed to study the transport of suspended sediment, so the data were available from approximately $z^+ > 40$. In addition, the particle concentration they had observed in the water column was very low, thus the one-way coupling situation might apply. This is, although the average particle concentration of suspended sediment is very low, there could be some regions with local particle clustering where the concentration is higher, and therefore the inter-particle collisions could have importance in these regions, and it might have a role in the average particle concentration. In this sense, the results of the simulations shown below will determine the applicability of one-way coupling for suspended sediment transport.

In order to compare with the experimental results presented by Breugem and Uijttewaal (2006) and Breugem (2012), simulations with the same Reynolds number $\mathrm{Re}_\tau = 500$ were performed. But, also simulations with lower Reynolds number ($\mathrm{Re}_\tau = 180$) were performed in order to analyse the adequate scaling for different flow Reynolds number. For both Reynolds numbers, we used a computational-domain of size $6H \times 3H \times H$, in the stream (x), span (y) and normal-wise directions (z), respectively (Fig. 1). This corresponds to 1080 × 540 × 180, in wall-units, for $\mathrm{Re}_\tau = 180$, and to 3000 × 1500 × 500 for $\mathrm{Re}_\tau = 500$. We used a grid of 96^3 nodes for $\mathrm{Re}_\tau = 180$, with uniform grid spacing in the x and y directions, which gives $\Delta x^+ \approx 11$ and $\Delta y^+ \approx 6$. A hyperbolic-tangent function with stretching factor of 1.7 was used for the grid-distribution in the wall-normal direction, which gives $\Delta z^+_{\mathrm{min}} \approx 0.4$ at the wall and $\Delta z^+_{\mathrm{max}} \approx 3.4$ in the middle of the channel. The same grid configuration was used for $\mathrm{Re}_\tau = 500$, with a grid of 256^3 nodes, which gives $\Delta x^+ \approx 12$, $\Delta y^+ \approx 6$, and $\Delta z^+_{\mathrm{min}} \approx 0.5$ at the wall and $\Delta z^+_{\mathrm{max}} \approx 3.6$ in the middle of the channel. The average time-steps for the fluid are roughly $t^+ \approx 0.033$ for $\mathrm{Re}_\tau = 180$ and $t^+ \approx 0.027$ for $\mathrm{Re}_\tau = 500$, in wall-units.

The particles were included into the simulation once statistically steady-state turbulent flow is reached. Initially, 10^6 particles were released in random position over the computational-domain, with their initial velocities equal to the fluid velocities interpolated at the centre of each particle. The particle diameter, in wall-units, is $\mathrm{Re}_p = d_p^+ = 3.47$, and the particle radius is $a^+ = 1.735$; particle-to-fluid density ratio is $\beta = 1.0367$; the Stokes number is $\mathrm{St} = t_p^+ = 0.693$, and the modified Stokes number is $\mathrm{St}_a = t_a^+ = 1.028$, giving the particle settling velocity of $w_s^+ = 0.236$, and thus, the modified particle Froude number $\mathrm{Fr}_a^2 = 4.4$. These particle parameters in wall-units are maintained for both Reynolds numbers.

3.2. Numerical experiments

Simulations with different configurations of forces with and without virtual wall are performed in order to analyse the effects of each configuration in the statistics of particle-motion. Table 1 summarises the simulations performed.

Two groups of simulations were performed: (i) the prefix `hRe-` corresponds to the flow with $\mathrm{Re}_\tau = 500$, and (ii) the prefix `lRe-`

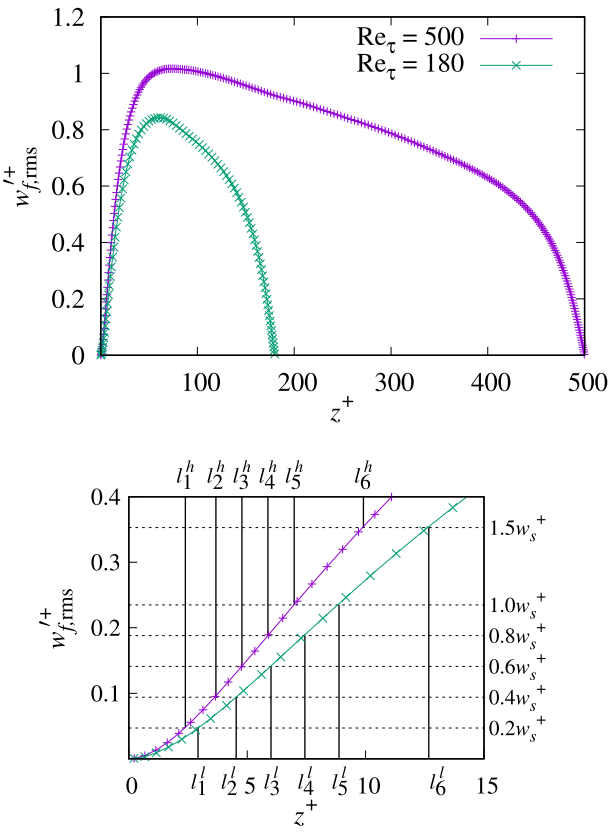

Fig. 4. The profiles of rms of fluctuating fluid velocity in wall-normal direction for Re_τ = 500 and 180: (up) shows the whole channel height and (down) shows a small region close to the bottom wall. The magnitudes are represented in wall-units.

to Re_τ = 180. The forces of drag, stress-gradient and added-mass are included by default in all simulations performed in this work. In the cases with suffix `-d`, it uses the default forces; cases with suffix `-l` the lift force is included; and cases with suffix `-gl` the gravity and the lift forces are included from the default cases. The cases with virtual wall are labelled by the suffixes `-v1`, `-v2`, `-v3`, `-v4`, `-v5` and `-v6` according to its position.

Fig. 4 shows the profiles of the rms of wall-normal fluctuating fluid velocity for both Reynolds number (Re_τ = 180 and 500). The positions of the virtual wall were selected in such a way that the ratio between the rms of wall-normal fluctuating fluid velocity at the centre of a particle in contact with the virtual wall and the magnitude of the particle settling velocity is equal to 0.2, 0.4, 0.6, 0.8, 1.0 and 1.5; or similarly, corresponding to the local particle Froude numbers (see Eq. (13)) which squared values are equivalent to 0.2, 0.4, 0.6, 0.8, 1.0 and 1.5. Fig. 4(down) shows a zoom in near-wall region with horizontal dashed-lines at mentioned values. These dashed-lines intersect the rms values at $l_i^h (i = 1, 2, \ldots, 6)$ distances from the wall, respectively, for Re_τ = 500, and at $l_i^l (i = 1, 2, \ldots, 6)$ distances from the wall, respectively, for Re_τ = 180. The detailed values of the distances, in wall-units, are shown in Table 2, where the position of the virtual wall is represented by z_r which is the distance measured from the bottom wall, and l is the position of the centre of a particle touching the virtual wall, also measured from the bottom wall.

To determine whether the simulations with particles have reached the statistically steady-state, the evolution of the number of particles in a region close to the bottom wall is computed. In this work, we limit this region close to the bottom wall, and it is referred to as "bottom layer" represented by Δz_b. The thickness of the bottom layer is set equal to the 0.5% of the height available for the centre of the particles: $\Delta z_b = 0.005(H - d_p)$ without virtual wall ($\Delta z_b^+ = 2.48$ for Re_τ = 500 and $\Delta z_b^+ = 0.89$ for Re_τ = 180), and it is slightly reduced with the presence of the virtual wall, $\Delta z_b = 0.005(H - d_p - z_r)$, which in wall-unit is $\Delta z_b^+ = 2.47 - 2.43$ for Re_τ = 500 and $\Delta z_b^+ = 0.88 - 0.83$ for Re_τ = 180. After the statistically steady-state for the number of particles in the bottom layer have been reached, the simulations were continued until sufficient uncorrelated data were collected for the several statistics of particle-motion.

Table 2
Simulations performed with virtual wall: the column z_r is the position of the virtual wall, the column l is the position of the centre of particles touching the virtual wall, and the column $\mathrm{Fr}_l^2(l)$ is the value of the local particle Froude number at l, see eq. (13). All numerical values are in wall-units. The superscript + was skipped to maintain clear the notation.

Cases	z_r	$l = z_r + a$	$\mathrm{Fr}_l^2(l)$
`hRe-v1`	$z_{r1}^h = 0.65$	$l_1^h = 2.38$	0.2
`hRe-v2`	$z_{r2}^h = 1.94$	$l_2^h = 3.67$	0.4
`hRe-v3`	$z_{r3}^h = 3.00$	$l_3^h = 4.74$	0.6
`hRe-v4`	$z_{r4}^h = 4.10$	$l_4^h = 5.83$	0.8
`hRe-v5`	$z_{r5}^h = 5.20$	$l_5^h = 6.94$	1.0
`hRe-v6`	$z_{r6}^h = 8.24$	$l_6^h = 9.98$	1.5
`lRe-v1`	$z_{r1}^l = 1.19$	$l_1^l = 2.92$	0.2
`lRe-v2`	$z_{r2}^l = 2.80$	$l_2^l = 4.53$	0.4
`lRe-v3`	$z_{r3}^l = 4.37$	$l_3^l = 6.00$	0.6
`lRe-v4`	$z_{r4}^l = 5.70$	$l_4^l = 7.43$	0.8
`lRe-v5`	$z_{r5}^l = 7.14$	$l_5^l = 8.87$	1.0
`lRe-v6`	$z_{r6}^l = 10.92$	$l_6^l = 12.66$	1.5

Table 3
Details of simulation time: the total simulation time performed, the period of statistically steady-state particle distribution and saving frequency of data in steady-state period for the particle statistics. The values are in wall-units.

Id	Simulation time	Steady-state	Saving frequency
`hRe-d/l`	25,000	15,000 – 25,000	250
`hRe-gl`	100,000	25,000 – 100,000	250
`hRe-v1/6`	25,000	15,000 – 25,000	250
`lRe-d/l`	18,000		
`lRe-v1/6`	18,000	10,800 – 18,000	180

The Table 3 shows the details of the simulation time for each case. The time for the simulations begins when the particles are released into the computational domain of the statistically steady-state turbulent flow previously obtained. The simulation time shown in the second column is composed of an initial transient period, followed by a statistically steady-state particle-distribution shown in the third column. The data from this steady-state are saved with the frequency shown in the last column. The saved data are used for the statistics of particles-motion.

3.3. Fluid and particle statistics

For the computation of particle statistics, N_s layers parallel to the top and bottom walls, and distributed non-uniformly along the wall-normal direction, are considered (Marchioli et al., 2008). For Re_τ = 500, N_s = 160 layers are used and N_s = 64 layers for Re_τ = 180. The layers are distributed using a hyperbolic-tangent function with a stretching factor of γ = 1.7 similar to those used in wall-normal grid-distribution for the solver of fluid motion. The position of the particle is defined by its centre, and thus, due to the geometric consideration, it is not possible to find particles in regions where the distance from the walls is lower than one particle radius. Therefore, the bottom layer starts at a distance equal to one particle radius from the bottom wall ($z_s(0) = a$) or from the virtual wall ($z_s(0) = z_r + a$), and the last layer ends at a

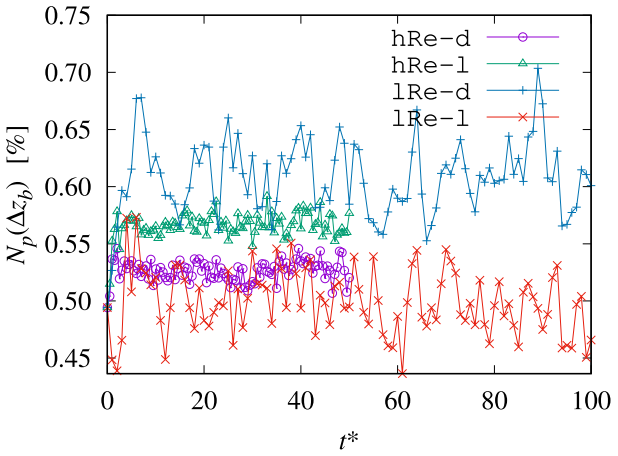

Fig. 5. Cases without gravitational force: percentage of particles in the bottom layer Δz_b along the simulation time.

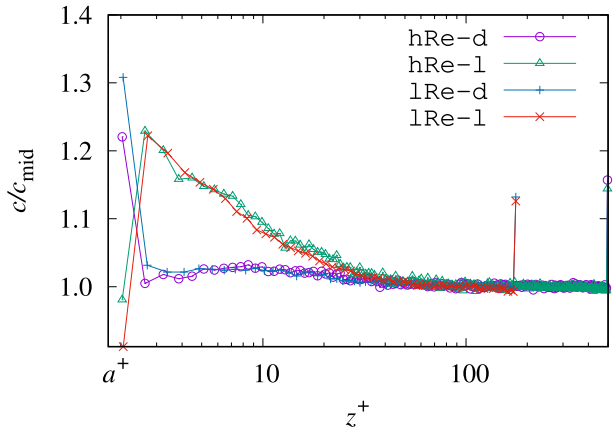

Fig. 6. Cases without gravitational force: particle concentration profile scaled by its value at $z = H/2$ (the middle of the channel). $c_{\text{mid}} = c(z = H/2)$.

distance equal to one particle radius from the top wall ($z_s(N_s) = H - a$). The thickness of the sth layer ($s = 1, 2, \ldots, N_s$) is:

$$\Delta z_s(s) = (H - d_p)\frac{\left[\tanh\left(\gamma\frac{N_s - s + 1}{N_s}\right) - \tanh\left(\gamma\frac{N_s - s}{N_s}\right)\right]}{\tanh(\gamma)}. \quad (21)$$

A particle belongs to a layer if its centre is located inside the layer. In each layer, the property is averaged over all particles belonging to that layer.

4. Results and discussions

This section shows the results obtained from the simulations together with some discussions. First, the results from the simulations without gravitational force are presented and is contrasted to the transport mechanism in gas–solid/liquid applications (see Section 4.1). Section 4.2 shows the results with gravity but without virtual wall. Then, an extensive analysis of the simulations with virtual wall is presented from Section 4.3: some averaged quantities are shown in Section 4.3, the near-wall particle clustering in Section 4.4, the quadrant analysis in Section 4.5, and finally some discussions about the particle-concentration in the near-wall region for different positions of virtual wall are presented in Section 4.6.

4.1. Without gravitational force

The first configuration analysed is the case without gravitational force (cases `hRe-d`, `hRe-l`, `lRe-d` and `lRe-l` from the Table 1). These configurations are analysed in order to evaluate the influences of the terms containing fluid-acceleration and the lift force on the particle-motion in the absence of gravitational force. Two sets of simulations: (i) one with fluid-acceleration terms (cases `hRe-d` and `lRe-d`), and (ii) another with both fluid-accelerations terms and lift force together (cases `hRe-l` and `lRe-l`), are performed for both flow Reynolds number.

In order to acquire the statistically steady-state for the particle motion, the amount of particles in the bottom layer is monitored along the simulation time, and is presented in Fig. 5. The simulation time is represented in outer-unit ($t^* = tu_\tau/H$) and the amount of particles is in percentage with respect to the initial amount of particles released (10^6 particles). Due to the initial random-distribution of particles, the initial amount of the particles in the bottom layer are approximately equal to the percentage of volume occupied by this layer (approximately 0.5%). From this initial value, it observes some accumulation of particles near the wall, obtaining values slightly larger than the initial particle amounts, and it oscillates around these values for the rest of the simulation.

Fig. 6 shows the particle-concentration profile scaled by its respective concentration in the middle of the channel: $c_{\text{mid}} = c(z = H/2)$. In the cases without lift force, slightly larger particle accumulations are observed very close to the bottom wall, but away of the first grid point, the particle-concentration is essentially uniform. When the lift force is included, the lift force prevents the particle accumulation on the bottom, but larger amount of particles is observed in the viscous sub-layer. From the buffer layer, the particle-concentration also becomes uniform.

For the computation of the particle momentum profiles, the drag force, stress-gradient and added-mass forces for each particle are evaluated using the particle velocity, and fluid velocities and their gradients at the particle position. Then these forces are averaged over the particles located in each layer. The diffusion and turbophoretic effects are evaluated after the profiles of the particle Reynolds stress tensor and concentration are obtained. Small oscillations in the profiles of particle motion are observed, which is somehow inevitable because of the difficulty to obtain a converged statistic profiles for the particles. In order to smooth these oscillations, the profiles are fitted by smoothing spline curves.

Fig. 7 show the particle momentum profiles for Reynolds numbers $\text{Re}_\tau = 500$ and 180. The Fig. 7(up) shows the streamwise profiles, and Fig. 7(down) the profiles in the wall-normal direction. It can be noticed that the major contributions are given by the turbophoretic effects, which are balanced by the stress-gradient force. The rest forces have secondary contributions. The diffusion effects are negligible due to the nearly uniform particle-concentration profiles. The small particle relaxation time allows the particles to follow almost perfectly the fluid motion. As a result, very similar average velocities between particles and fluid are observed with negligible drifts, and also there are very similar Reynolds stresses between particles and fluid. Hence, the drag and added-mass forces are negligible. The profiles corresponding to the Reynolds number $\text{Re}_\tau = 180$ have a little smaller values, but they present identical behaviour compared to the simulation with $\text{Re}_\tau = 500$.

When the lift force is included into the simulations (Fig. 8), the particle momentum profiles are very similar to the cases without lift force. The dominant forces are also the stress-gradient and turbophoresis, which balance each other. The diffusion effects are still negligible besides of the particle accumulation in the viscous sub-layer (see Fig. 6), *i.e.*, this particle accumulation is not high enough thus the diffusion effects are damped by the small near-wall turbulence. The appreciable differences compared to the cases without lift force is that, in wall-normal direction, the drag force arises to balance the lift force.

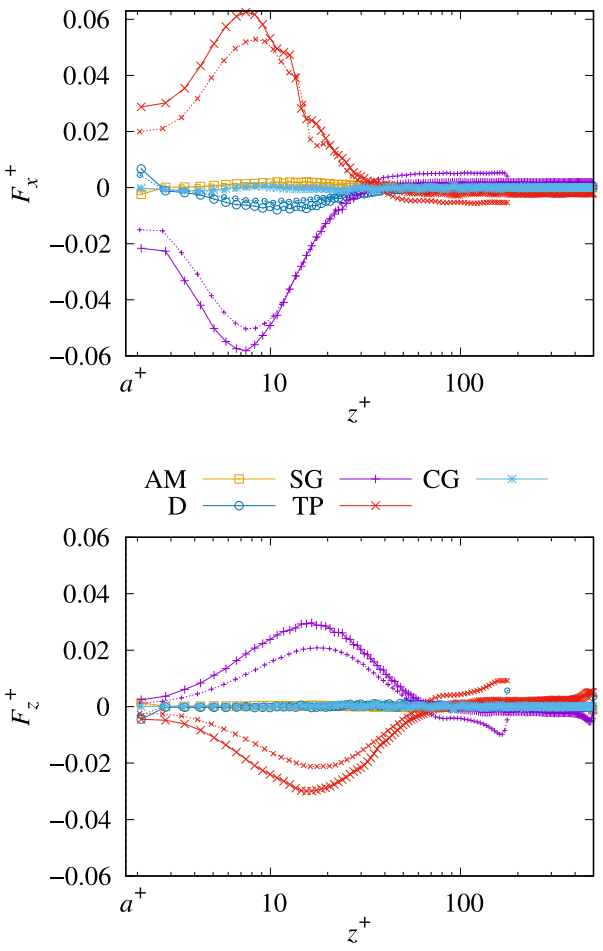

Fig. 7. Cases hRe-d, lRe-d: particle momentum profiles for $Re_\tau = 500$ (continuous curves with larger symbols) and $Re_\tau = 180$ (dotted curves with smaller symbols), in wall-units: streamwise (up), wall-normal direction (down). AM: added-mass force, SG: stress-gradient force, TP: turbophoretic effect, D: drag force, CG: diffusion effect.

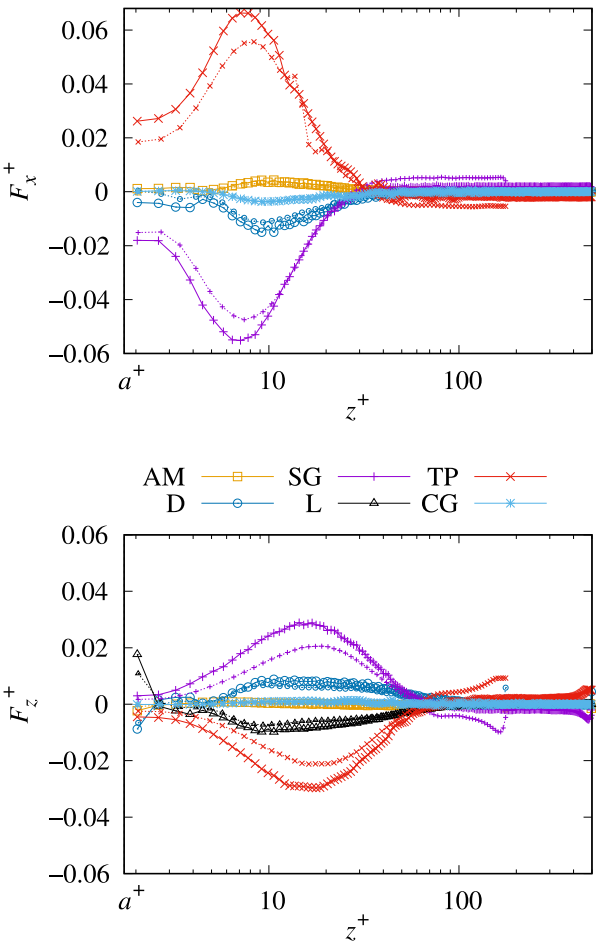

Fig. 8. Cases hRe-l and lRe-l: particle momentum profiles for $Re_\tau = 500$ (continuous curves with larger symbols) and $Re_\tau = 180$ (dotted curves with smaller symbols), in wall-units: streamwise (up), wall-normal direction (down). D: drag force, SG: stress-gradient force, AM: added mass force, CG: diffusion effect, TP: turbophoretic effect, L: lift force.

Particularly, the lift force pushes the particles towards the wall. This is because the particles mostly have positive slip-velocity (particle velocity larger than the fluid streamwise velocity), *i.e.*, from Eq. (4), the sign(G) is mostly positive which is the characteristic to the channel flow, J becomes close to the value 2.255 where the lift force is identical to the Saffman lift formula (Wang et al., 1997), and positive slip-velocity turn the lift force to be negative (force towards the wall).

Although the particles are almost following the fluid motion, small streamwise velocity lags of the particles, $U_f - U_p$, are observed. This can be observed in Fig. 9, where the velocity magnitudes are scaled by the friction velocity, which means that the velocity lags have an order of magnitude smaller than the friction velocity. The average relative velocity is further smaller because the drift velocity which is almost similar to the velocity lags with opposed sign is included: $U_{rel} = U_f + \left\langle u'_f \right\rangle_p - U_p$. This is, the particles are mostly located in the negative fluid velocity fluctuation (negative drift velocity), thus the particle velocity is slightly larger than the local fluid velocity. This is in accordance with the positive slip-velocity, and also to the negative drag force observed in Fig. 8(up), *i.e.*, the velocity difference between the fluid and the particle is used for the drag force, thus it is opposed to the slip velocity. Also, the particles are mostly located in upward fluid motion, so the drag force is upward in wall-normal direction. Despite

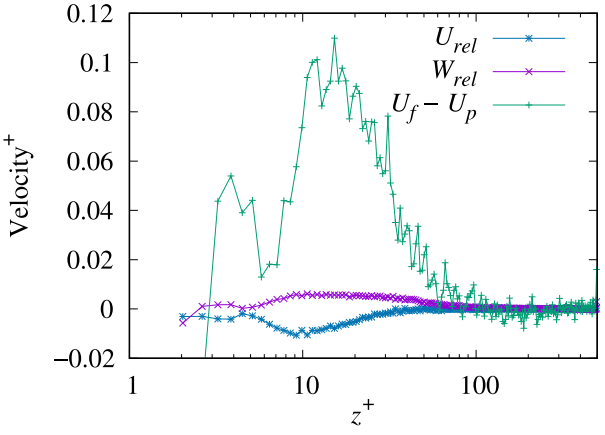

Fig. 9. Case hRe-l: Velocity differences. $U_{rel} = \langle u_f - u_p \rangle_p$: average velocity differences between the fluid and the particles in streamwise direction, $W_{rel} = \langle w_f - w_p \rangle_p$: in wall-normal direction, $U_f - U_p$: streamwise velocity lag.

all this, the average velocity differences between the particles and the fluid, in both streamwise and wall-normal directions, have an order of magnitude smaller than the velocity lags. Therefore, the drag force in

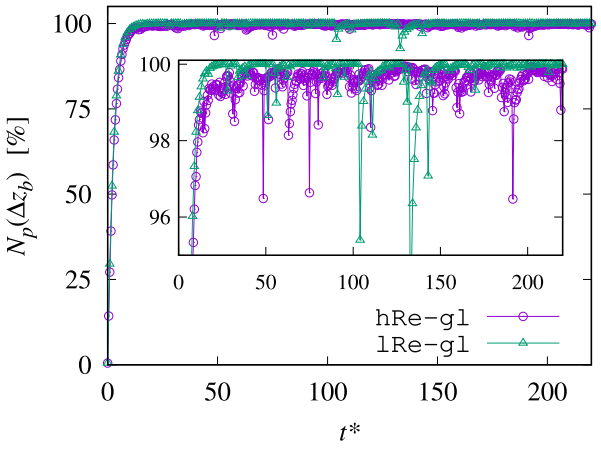

Fig. 10. Cases `hRe-gl` and `lRe-gl`: percentage of particles in the bottom layer Δz_b along the simulation time.

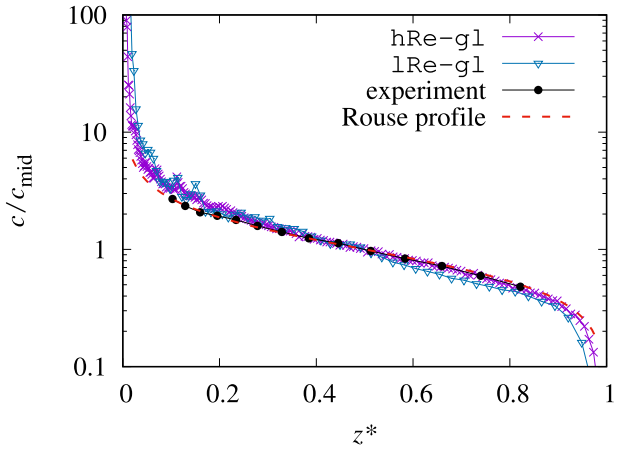

Fig. 11. Comparison: particle-concentration profiles from the simulations with lift force, and from experiments by Breugem and Uijttewaal (2006) and Breugem (2012). The particle-concentration profiles c are scaled by their respective particle-concentration in the centre of the channel $c_{\text{mid}} = c(H/2)$. The horizontal axis represents the wall-normal direction z which is scaled by the channel height H, denoted by z^*.

streamwise has only secondary effect, and in the wall-normal direction, it balances the small lift force.

The profiles corresponding to the Reynolds number $\text{Re}_\tau = 180$, which are plotted in Fig. 8, present identical behaviour compared to the simulation with $\text{Re}_\tau = 500$.

These results suggest that the inclusion of the stress-gradient force in the particle momentum equation is essential. If this force were not included, the drag force and the diffusion effects would be larger in order to balance the turbophoresis. This means that, a much higher particle-concentration would be observed near the wall, and the dispersion of the particles due to the drift would be higher. This is contrasted to the gas–solid/liquid applications where the forces associated to the fluid-acceleration term are negligible due to the high particle-to-fluid density ratio.

4.2. With gravity and lift force

In this Section, the results of the simulations including the gravity and lift force are presented for both Reynolds number: the case identification `hRe-gl` corresponds to $\text{Re}_\tau = 500$ and the case `lRe-gl` to $\text{Re}_\tau = 180$ (see Table 1). Fig. 10 shows the amount of particles in the bottom layer Δz_b along the simulation time for both Reynolds number. From the initial random particle distribution, a very large amount of particles is deposited in a short time, only remaining a small proportion in suspension. Similar initial slopes of the graphs are observed for both Reynolds numbers, meaning that the initial deposition rates are comparable when the wall-unit scaling for the particles is used for different flow Reynolds numbers. In the figure, there is a zoom to show values close to 100 in the percentage of amount of particles in the bottom layer. The deposition of more than 99% of particles in average within a very small region (0.5% of the channel volume) are observed for both Reynolds numbers.

Fig. 11 shows the particle-concentration profiles, from the simulation with lift force for both Reynolds numbers, $\text{Re}_\tau = 500$ and 180, and from the experiments done by Breugem and Uijttewaal (2006) and Breugem (2012). These profiles are also compared to the analytical solution from advection-diffusion model, known as Rouse profile.

The transport of suspended sediment can be modelled by an averaged advection–diffusion equation, where the downward sediment flux due to the particle settling velocity is in equilibrium with the upward flux due to the turbulent diffusion. The particle turbulent diffusion (D_t) is normally expressed as being proportional to the turbulent eddy-viscosity (ν_t), which can be assumed to have a parabolic profile in a turbulent open channel flow. An analytical solution of the averaged advection–diffusion equation can be obtained once a reference particle-concentration at a reference height is provided. This solution, known as Rouse profile (Rouse, 1939), can be expressed as:

$$\frac{c}{c_{\text{mid}}} = \left[\frac{H-z}{H-z_{\text{mid}}}\cdot\frac{z_{\text{mid}}}{z}\right]^{\text{Sc}_t w_s/\kappa u_\tau}, \tag{22}$$

where the reference height, in this work, is set equal to the middle of the channel-height, $z_{\text{mid}} = H/2$, with the reference concentration $c_{\text{mid}} = c(z_{\text{mid}})$; Sc_t is the turbulent particle Schmidt number defined as the ratio between the fluid turbulent eddy-viscosity and the turbulent particle diffusion, and $\kappa = 0.41$ is the von Kármán constant. Although, the reference height is normally considered as a few diameters of particle from the channel bed, the reference height in the work of Breugem and Uijttewaal (2006) is set at $z/H = 0.25$, because the experimental results were more reliable in higher water column. In this work, the reference height is set in the middle of the channel ($z_{\text{mid}}/H = 0.5$), and all particle-concentration profiles are scaled with its respective concentration at the middle of the channel. As the assumption of the Rouse profile is one-way coupling, as well as the simulations performed in this work, only the relative concentration can be adequately determined. In this sense, the reference height is arbitrary, and since the focus of this work is suspended sediment transport, this reference height is set above the buffer-layer. The best-fit value of turbulent particle Schmidt number for the agreement between the Rouse profile and the experimental data gives $\text{Sc}_t = 0.79$. The Rouse profile using this best-fit turbulent particle Schmidt number is also shown in Fig. 11. Very good agreements are observed between the simulation results and the experimental data. But, close to the wall, the results of the simulations are moving far away from the Rouse profile. Actually, close to the bottom wall the point-particle one-way coupling approach inevitably over-predicts the particle concentration and thus the simulation results would not be reliable in this region.

Highly intermittent particle resuspensions can be observed in Fig. 10. This intermittency in the particle suspension generates large oscillations in the particle statistics, and makes it difficult to obtain converged statistics for the particles, therefore it was required a large amount of data.

In order to compute the diffusion and the turbophoretic effects for the particle momentum profiles, the gradient of the particle-concentration profile has to be evaluated. It is possible to determine this particle-concentration gradient directly from the derivative of the particle-concentration profile (from Fig. 11), but this gradient

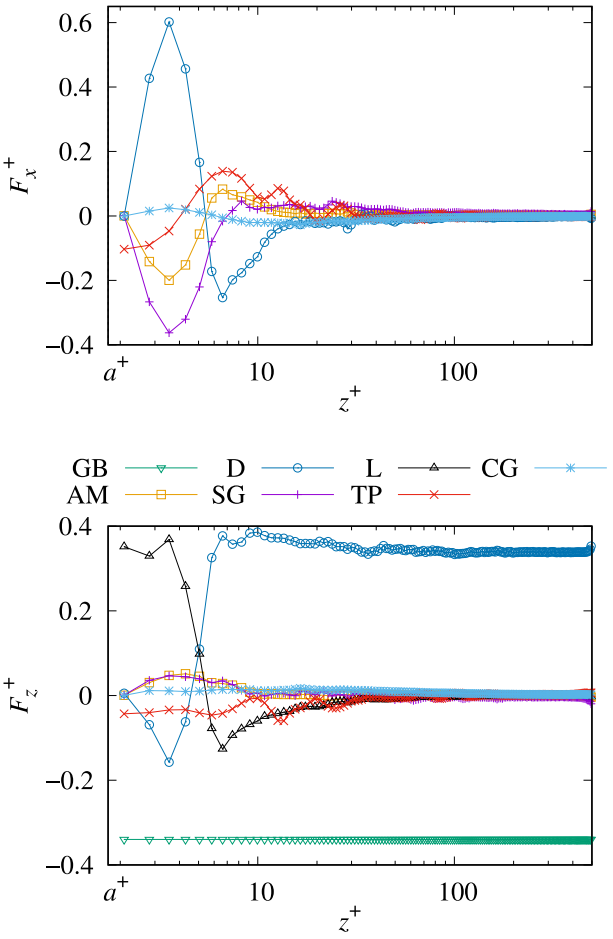

Fig. 12. Case `hRe-gl`: particle momentum profiles for Re_τ = 500, in wall-units: streamwise (up), wall-normal direction (down). GB: gravitational force, L: lift force, D: drag force, SG: stress-gradient force, AM: added mass force, CG: diffusion effect, TP: turbophoretic effect, L: lift force.

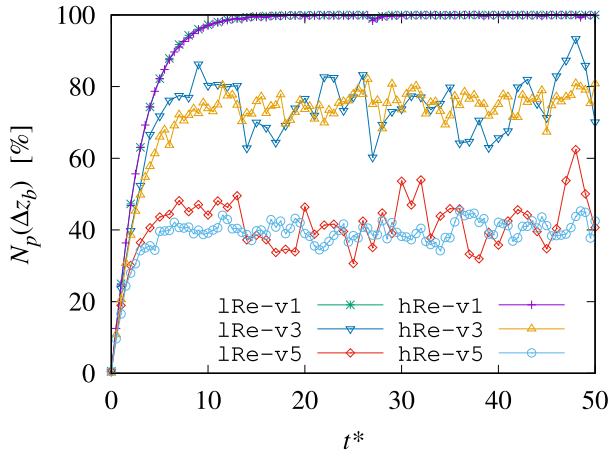

Fig. 13. Cases with virtual wall: percentage of particles in the bottom layer Δz_b along the simulation time.

would be over-predicted close to the bottom wall due to the unrealistically high particle accumulation. In addition, the derivative of a not smooth function adds higher oscillations. On the other hand, if this gradient is computed from the derivative of the Rouse profile, then this would be under-predicted close to the bottom wall because of the restricted assumption in the formulation of the Rouse profile. This is, either computations would show unreliable results near the bottom wall, but both would also give similar results away from the wall. Here, the derivative of the Rouse profile is adopted just because of the non-oscillated behaviour.

Fig. 12 show the profiles of particle momentum: (up) in streamwise, and (down) in wall-normal direction, from the simulation with lift force for Re_τ = 500. The drag force in streamwise (Fig. 12(up)) is dominant within the viscous sub-layer, and it balances the sum of both the added-mass and the stress-gradient forces. The drag force has positive value in the viscous sub-layer, and it becomes negative in the buffer-layer and above. Although, a large particle-concentration gradient is present close to the wall, the diffusion effects are damped by the reduced fluid turbulence in this region.

In wall-normal direction (Fig. 12(down)), the gravitational force acts on the particles towards the bottom wall with constant value. The lift force balances the gravitational force in the viscous sub-layer; in the buffer layer, this force becomes slightly negative and pushes the particles towards the bottom wall, but above the viscous sub-layer, it quickly drops to zero. Similarly to the case without gravitational force, the negative value of the lift force in the buffer layer is associated with the positive slip-velocity and also to the positive velocity-shear: the falling particles have higher streamwise velocity than the fluid velocity, so for these falling particles, the lift force contributes to their movements towards the wall. This negative lift force in the buffer layer is also observed by Zeng et al. (2008) in their fully resolved simulation of a stationary finite-sized particle in wall turbulent flow. Once the lift force becomes negligible, the drag force emerges, balancing the gravitational force in the rest of the channel height. Other forces have an order of magnitude smaller compared to the gravitational and the drag forces. It is worth mentioning that the particle size used in this work is comparable to Kolmogorov length-scale, hence the lift force model for a small particle Reynolds number might not strictly applicable. However, Zeng et al. (2009) showed that for the particle sizes comparable to the Kolmogorov length-scale, the order of magnitude of the lift force for finite-sized particles was not very different from that obtained by Wang et al. (1997) for low particle Reynolds number used in this work. As above the buffer-layer the contribution of the lift force is negligible, other lift force model which has similar order of magnitude would not change the dynamics of suspended particles. In addition, in the viscous sub-layer, the inclusion of any lift force model without considering the inter-particle interaction would fail to represent the complex mechanism in the near-wall region.

4.3. With virtual wall

In this section, the simulation results using the virtual wall are presented. To analyse the effects of the position of virtual wall on the dynamics of the suspended particles, the results from the simulations with virtual wall in several positions are compared to each other, and against the results using lift force (Section 4.2), and also with the experimental data. The forces included into the simulations with virtual wall were the drag, stress-gradient, added-mass, and gravitational forces. The virtual walls are placed in the viscous sub-layer or slightly above it, and so the particles are mostly above the viscous sub-layer, where the lift force is negligible. For this reason, the lift force was excluded in the simulations with virtual wall. See Table 2 to identify the cases (with the position of the virtual wall) shown in this section. For the clarity of the figures, only some relevant cases are presented.

Fig. 13 shows the amount of particles in the bottom layer Δz_b (approximately 0.5% of the channel volume) along the simulation time for cases corresponding to three positions of virtual wall and both Reynolds numbers. Similar initial slopes of the graphs are observed in all cases and therefore the initial deposition rates are comparable regardless of the position of the virtual wall and the Reynolds number.

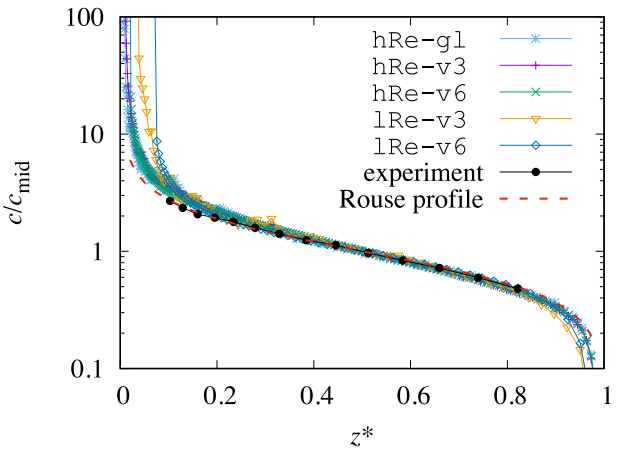

Fig. 14. Comparison: particle-concentration profiles from the simulations with virtual wall, and from experiments of Breugem and Uijttewaal (2006) and Breugem (2012). The particle-concentration profiles c are scaled by their respective particle-concentration in the centre of the channel $c_{\mathrm{mid}} = c(H/2)$. The horizontal axis represents the wall-normal direction z which is scaled by the channel height H, denoted by z^*.

From the initial random particle distribution, in a short time, different amounts of particles are deposited depending on the position of the virtual wall. The cases with the lowest position of virtual wall (identified with suffix `-v1`) have higher particle accumulation on the virtual wall. As the virtual wall is positioned further away from the bottom wall, the amount of particle deposited is reduced, which means that there are more particles in suspension. It can be noticed that the cases with different Reynolds number, but same suffixes, give similar proportions of deposited particles. Thus, the positions of virtual wall with similar local particle Froude number present similar proportions of accumulated particles on the wall.

Fig. 14 shows the particle-concentration profiles of the simulation with virtual wall for both Reynolds numbers, together with the result with lift force (showed in the previous section), the experimental data, and the Rouse profile (the reference height is set equal to the middle of the channel-height, $z_{\mathrm{mid}} = H/2$, with the reference concentration $c_{\mathrm{mid}} = c(z_{\mathrm{mid}})$ similar to Fig. 11). Two cases were selected for each Reynolds number, one corresponding to an intermediate position and the other to the uppermost position of the virtual wall. Larger simulation time is required for the convergence of particle motion statistics in the two cases corresponding to the lower positions of the virtual wall (cases with the suffix `-v1` and `-v2`), due to the reduced proportions of suspended particles. This is contrasted to the simulations in which the virtual wall is placed higher.

The particle-concentration profiles are scaled with the respective concentration at the middle of the channel, denoted as $c_{\mathrm{mid}} = c(z = H/2)$, so all concentration profiles become one at the middle of the channel. In addition, the wall-normal distance is scaled by the channel height H; in this way, flows with different Reynolds numbers can be compared to each other. Both simulations with lift force and with a virtual wall (irrespective of its position) give essentially the same particle-concentration profile above a certain distance from the wall, *e.g.*, $z^* = z/H > 0.1$. The simulation with low Reynolds number $\mathrm{Re}_\tau = 180$ shows some deviation close to the bottom wall because the virtual wall in this case is placed inside the buffer layer.

Although Fig. 13 shows different amounts of particles deposited on the virtual wall depending on their position, the relative particle-concentration in Fig. 14 shows almost identical profiles above the buffer layer, regardless of the position of the virtual wall, and they agree very well with the profile from experiments (Breugem, 2012). Thus, by using the virtual wall, it is possible to obtain adequate relative particle-concentration profile above the buffer-layer without taking into account the complex interactions present in the near-wall region.

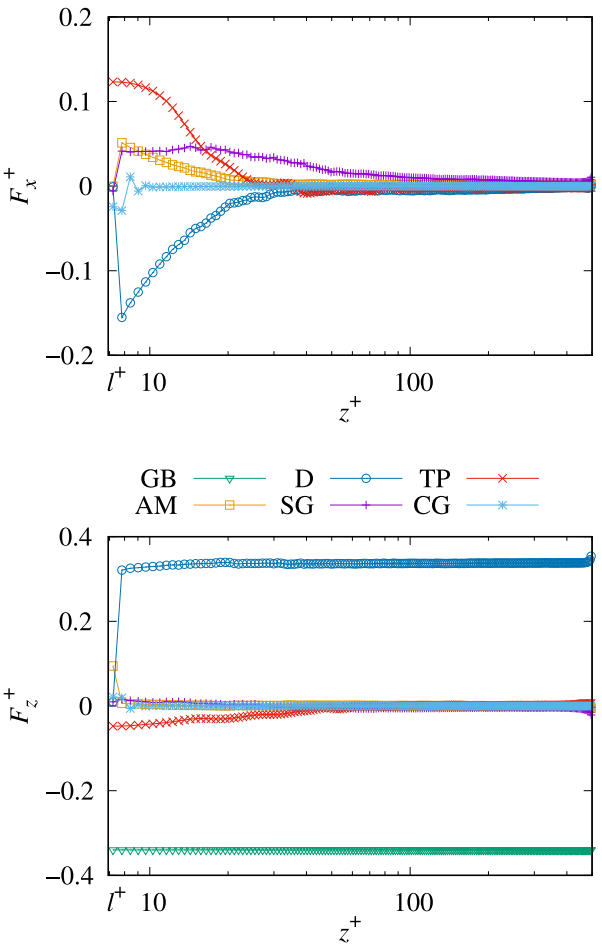

Fig. 15. Case `hRe-v5`: particle momentum profiles, in wall-units: streamwise (up) and wall-normal direction (down). GB: gravitational force, D: drag force, SG: stress-gradient force, AM: added mass force, CG: diffusion effect, TP: turbophoretic effect.

In the following, the different statistics of suspended sediment motion are presented and discussed.

Fig. 15 shows the particle momentum profiles from the simulation with virtual wall for $\mathrm{Re}_\tau = 500$, corresponding to the case `hRe-v5`. Due to the presence of the virtual wall, the first data points of the simulations are shifted a distance l (for this specific case $(l_5^h)^+ = 6.94$, see Table 3) from the bottom wall. The drag force and turbophoretic effect in streamwise (Fig. 15(up)) are revealed to be important and others (the added mass, stress-gradient and diffusion) are smaller but still can contribute to the particle momentum. In wall-normal direction (Fig. 15(down)), the gravitational force is balanced by the drag force; and other forces have at least one order of magnitude smaller. Similar profiles are obtained from simulations with different positions of the virtual wall and different Reynolds number. Furthermore, when this figure and Fig. 12 (shown in Section 4.2 for the case with lift force) are restricted to the region from the buffer layer ($z^+ \gtrsim 10$), both figures show very similar contributions of the different forces.

4.3.1. Average velocity

Fig. 16 show the particle velocity profiles, from the simulation with lift force, from the simulations with virtual wall, and the experimental data (Breugem, 2012): in streamwise (Fig. 16(up)), and in wall-normal direction (Fig. 16(down)); also, the fluid velocity profile is shown as a reference.

In streamwise direction (Fig. 16(up)), away from the bottom wall and approximately $z^+ > 40$ (region where the experimental data were

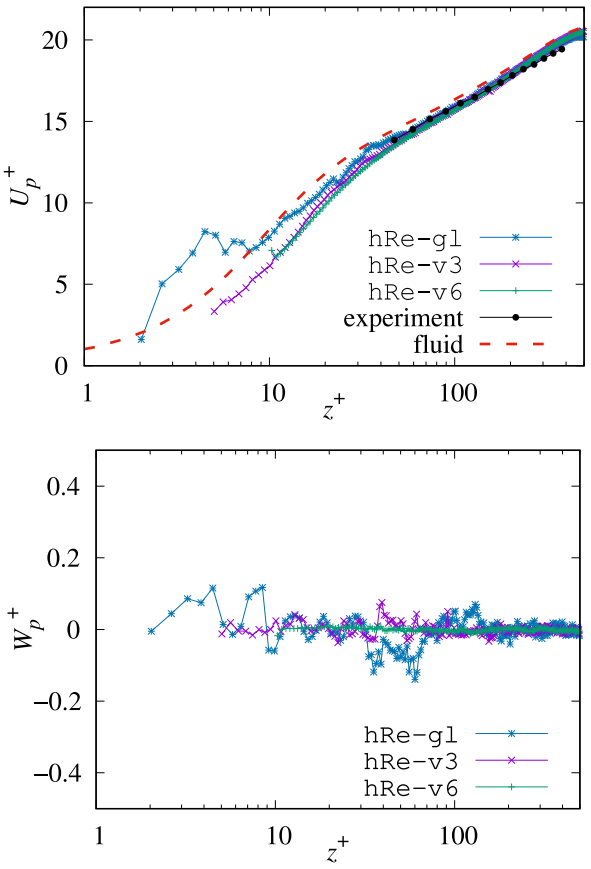

Fig. 16. Particle velocity profiles: (up) streamwise, (down) wall-normal direction.

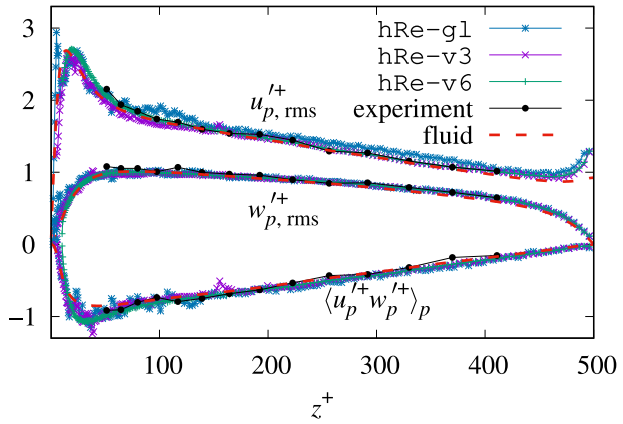

Fig. 17. Components of particle Reynolds-stress tensor.

available), very similar results are obtained in all cases simulated, and agree very well compared to the experimental data. The simulations with virtual wall located in different positions, give almost the same particle velocity profiles in the whole channel. In the channel height, the particles lag behind the fluid velocity. But, in the case with lift force and without the virtual wall, larger particle velocity compared to the fluid velocity is observed in the viscous sub-layer. This was previously noticed by several researchers from their experimental results, for instance see Rashidi et al. (1990), Kaftori et al. (1995), Nezu and Azuma (2004) and Muste et al. (2009), among others. The differences observed in the particle velocities close to the bottom between the simulations results are clearly due to the presence of the virtual wall. But this does not mean that one of them is the correct one and the others are not. Even though the simulation with lift force shows good qualitative agreement for the particle velocity compared to the experimental results from the literature, actually this simulation fails to represent the core physics close to the bottom wall, which is the inter-particle interaction due to the high particle concentration. On the other hand, the presence of the virtual wall can interfere with the motion of the particles in the near-wall region, but above a certain distance, let say $z^+ > 40$ or above the buffer-layer, regardless of the virtual wall position, or even more, regardless of the way the particles have been suspended, they show very similar statistics of particle motion.

In wall-normal direction (Fig. 16(down)), all results show nearly zero average velocities. This means that the particle motion has reached a statistically steady-state in all simulations performed. In simulations with virtual wall, the statistically steady-state was reached in relatively short simulation time, but in the simulation with lift force, it had to collect large amounts of data because of the large intermittent behaviour of the particle motion.

4.3.2. Turbulence

Fig. 17 shows the profiles of three relevant components of the particle Reynolds-stress tensor: expressed in the form of the rms of the fluctuating particle velocity in streamwise and wall-normal directions, and the particle Reynolds shear-stress, from the simulations with virtual wall and with lift force, and these are compared against the experimental data. On top, the same components of the fluid Reynolds-stress tensor are also plotted. Almost the same results are obtained from the simulations, whether it is used the lift force model or the virtual wall, and they agree very well compared with the experimental results. The components of particle Reynolds-stress tensor are slightly above of the corresponding components of fluid Reynolds-stress tensor. Larger differences are observed in the buffer layer, where the peak of the particle streamwise fluctuation is a little shifted from the fluid fluctuation, and the particle Reynolds shear-stress has a larger peak (in absolute value) compared to the fluid Reynolds shear-stress. But, from $z^+ > 50$, where the experimental data is available (Breugem, 2012), there are no appreciable differences between the particle and fluid Reynolds stresses. Breugem (2012) had noticed similar results from his experiments: slightly larger particle Reynolds stresses compared to the fluid Reynolds stresses were observed, but he had also mentioned that there is no consensus in the literature whether one should be larger than the other given the sensitiveness of the experimental errors.

Fig. 18 shows the particle drift velocity in streamwise and wall-normal directions: $u_d = \left\langle u_f' \right\rangle_p$ and $w_d = \left\langle w_f' \right\rangle_p$. The particle drift velocity is the average of the fluid velocity fluctuations at the particle location, and it is related to the particle flux due to the turbulent diffusion (Simonin et al., 1993). The results from the simulations with lift force and virtual wall are plotted against the experimental result. Breugem (2012) had mentioned that the wall-normal drift velocity obtained in his experiments might have some bias error, and it had not been able to determine the small drift velocity, so the wall-normal drift velocity from the experiments was corrected using the particle settling velocity. The particles are located in the upward fluid velocity fluctuation, which means that the fluid turbulence is responsible for the upward particle flux and balances the downward sediment movement due to the gravitational effect. The negative streamwise drift velocity means that the particle velocity lag the fluid velocity (observed in Fig. 16), and this drift velocity is also equivalent to the difference between the particle and fluid average velocities.

All results obtained from the simulations with virtual wall, each wall located in a different position, show very similar results regardless of their positions, and agree very well compared to the experimental results. On the other hand, the simulations with lift force model give good qualitative results in the viscous sub-layer and buffer-layer. There was no reliable experimental data in these regions (Breugem, 2012); but, the results in the outer layer are very similar to those obtained

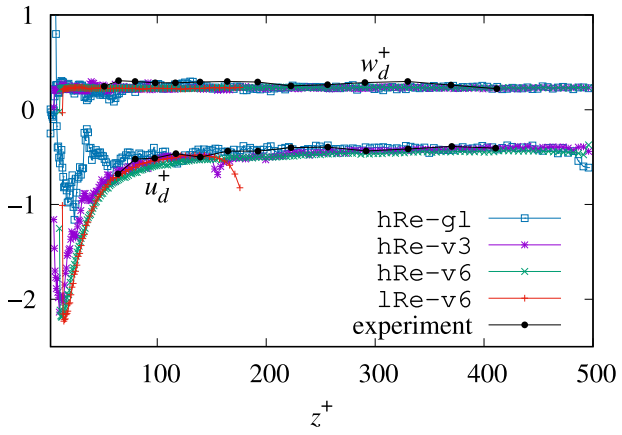

Fig. 18. Particle drift velocity.

using virtual wall, and also, agree very well compared to the experimental results. This means that, once the particles are brought to a distance from the bottom where the wall-normal velocity fluctuations of the fluid become of the same order as the particle settling velocity (or local particle Froude number in order of $\mathcal{O}(1)$), these particles have on average similar motions regardless of how they have been brought into suspension. In this sense, the virtual wall is very effective in relocating the particles to those regions. The details of the particle distribution in different fluid region is analysed in the next sub-section.

4.4. Particle clustering in the near-wall region

Fig. 19 shows the flow visualisation with particles from the simulations: (i) top: the simulation with lift force (case `hRe-gl`), (ii) middle: the simulation with virtual wall at $(z_3^h)^+ = 3.00$ (case `hRe-v3`), and (iii) bottom: the simulation with virtual wall at $(z_6^h)^+ = 8.24$ (case `hRe-v6`). The flow visualisations correspond to the instantaneous streamwise fluid velocity fluctuations at horizontal planes restricted to a horizontal window with size 1500 × 750, in wall-unit. These horizontal planes are separated the following distances from the bottom wall: a particle radius $a^+ = 1.74$ for the case `hRe-gl` (top), $(l_3^h)^+ = 4.74$ for the case `hRe-v3` (middle), and $(l_6^h)^+ = 9.98$ for the case `hRe-v6` (bottom), *i.e.*, the particles which are in contact with the bouncing-wall (the bottom wall or the virtual one) will see the fluctuating streamwise fluid velocity shown in these images. The horizontal direction of the images is the flow streamwise direction and the vertical is the flow spanwise direction. The flow direction is from the left to the right of the images. Black circles (dots) represent particles belonging to a layer with thickness $\Delta z^+ = 2.5$ from the mentioned horizontal planes in upward direction. The negative fluctuating fluid velocity (instantaneous velocity lower than the average) are represented by blue, and the positive fluctuations (instantaneous velocity higher than the average) are represented by red.

Apparently, there are more particles (in the bottom layer) as the virtual wall is placed farther away from the bottom wall. But on the contrary, the actual number of particles is lower: for instance, in the figures shown, there are 140,799 particles in the case `hRe-gl` from the simulation with lift force model; 52,094 particles in the case `hRe-v3` from the simulation with the virtual wall in the intermediate position, and 46,801 particles in the case `hRe-v6` from the simulation with the highest position of the virtual wall. In Fig. 19(up), a strong non-uniform particle distribution is observed. This is, the particles are concentrated in elongated filament-like structures, also known as bottom streaks, observed by several researchers (for instance see Rashidi et al. (1990), Kaftori et al. (1995), Narayanan et al. (2003) and Breugem (2012)). With the presence of the virtual wall (Fig. 19(middle) and

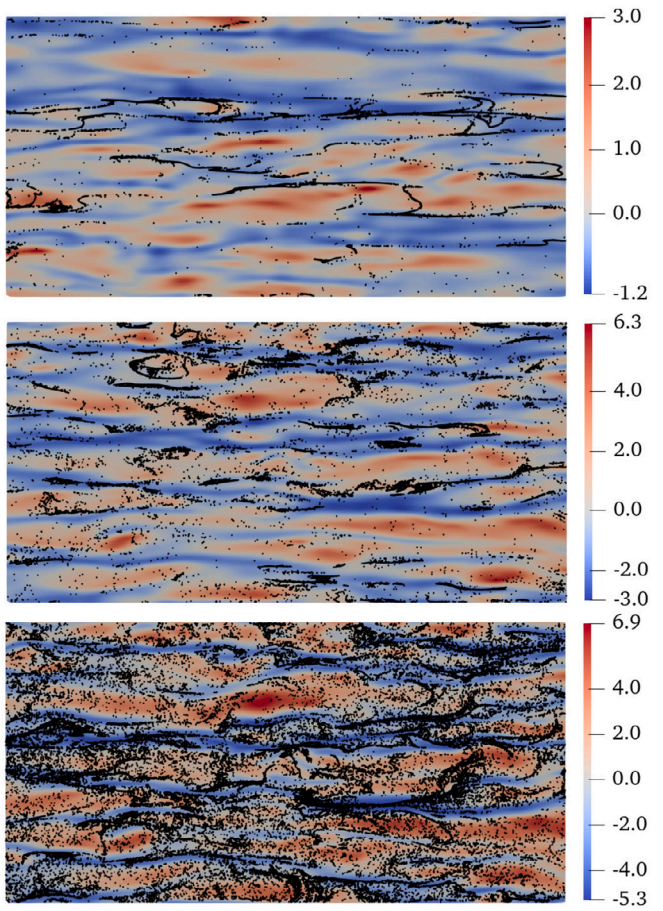

Fig. 19. Flow visualisations in horizontal planes at distances: (top) $a^+ = 1.735$ (case `hRe-gl`), (middle) $(l_3^h)^+ = 4.74$ (case `hRe-v3`), and (bottom) $(l_6^h)^+ = 9.98$ (case `hRe-v6`), from the bottom wall, restricted to a window with 1500 × 750 (in wall-unit) for Reynolds number $\mathrm{Re}_\tau = 500$ at $t^+ = 25{,}000$. The colour gradient from blue to red corresponds to the value of fluid streamwise velocity fluctuation. Black circles (dots) correspond to the particles located in the layer with thickness $\Delta z^+ = 2.5$ from the mentioned horizontal plane in upward direction. The flow direction is from left to right. (For interpretation of the references to colour in this figure legend, the reader is referred to the web version of this article.)

(down)), the filament-like structures are progressively diffused as the virtual wall is placed farther away from the bottom wall.

The clustering of the particles can be characterised by the Cumulative Density Function (CDF) of distances between particles, which is defined as $\mathrm{CDF}(r) = \mathrm{P}(R \leqslant r)$, where P is the probability that the random variable R takes on a value less than or equal to the distance r. Fig. 20(up) shows the CDF of distances between the particles located in the layer with thickness $\Delta z^+ = 2.5$ from the bouncing-wall. The distances r between particles are scaled by the largest representative distance between two particles, which is the half of the spanwise dimension ($L = L_y/2 = 1.5H$). Fig. 20(up) also shows two lines with different slopes denoted by D_2 which is known as correlation dimensions. The correlation dimension gives a measure of the dimension of the clusters (Monchaux et al., 2012), and is defined as the slope of the CDF of distance between particles in the log–log graph, which can be expressed as:

$$D_2(r) = \frac{d(\ln \mathrm{CDF})}{d(\ln r)}. \tag{23}$$

For instance, when particles are randomly distributed in a plane then the correlation dimension is $D_2 = 2$, indicating that the particles are distributed in two-dimensional space; if the particles are distributed in several filaments then: (i) D_2 is between 1 and 2 for distances larger

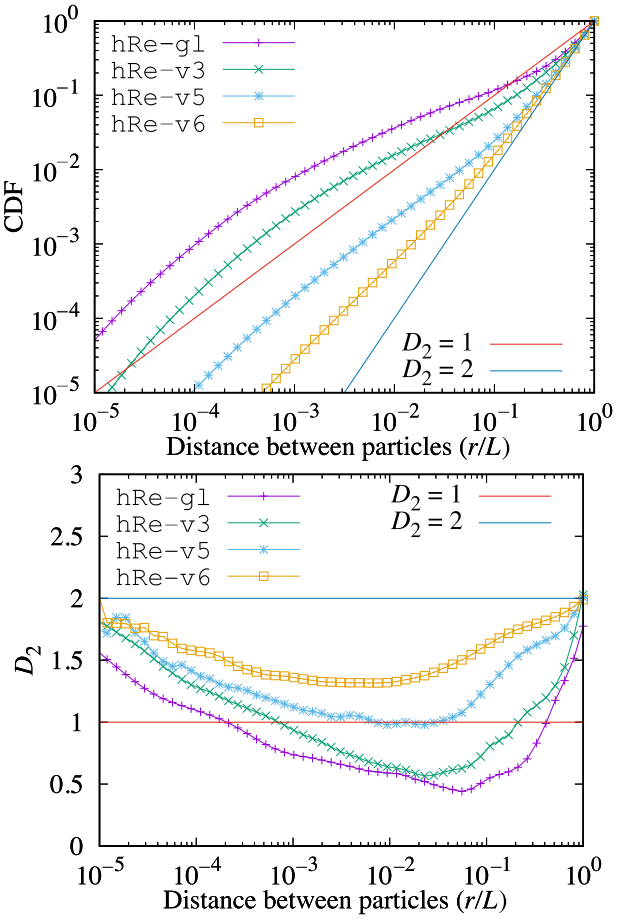

Fig. 20. (up) Cumulative Density Function (CDF) of distances between particles in near-wall region; (down) Correlation dimension of the particle distribution near the bottom wall for $\mathrm{Re}_\tau = 500$.

than the separation of the filament; (ii) D_2 approaches to 1 for distances smaller than the separation of the filament and larger than the thickness of the filament; and, (iii) D_2 approaches to 2 for distances smaller than the thickness of the filament.

The correlation dimensions D_2 of the particles in the same layer near the bottom wall are plotted in Fig. 20(down). Although, the case with lift force model, shows the filament-like structures of the particle distribution, there are regions inside the filaments where the particles are highly concentrated (see Fig. 19-up). This is the reason that there are values less than 1 for D_2, as shown in Fig. 20(down). As the simulations were done considering the particle as point-wise, it would not guarantee that two or more particles do not occupy the same space at the same time. In this sense, by considering only the fluid–particle interaction would not be enough to represent the complex physics near the bottom wall, and it would necessarily require the inclusion of inter-particle interactions. Actually, the particles are resuspended due to the complex fluid–particle and inter-particle interactions, which can be represented in a simple way by the virtual wall.

Although the particle distribution becomes more uniform as the virtual wall is placed farther away from the bottom wall, as in the case `hRe-v5` of Fig. 20(down), the one-dimensional distribution associated to the filament-like structures is diffused but still mildly maintained. In addition, the probability to locate particle pairs in distances smaller than the particle diameter when the virtual wall is located higher is further reduced, thus the point-particle approach would become more adequate.

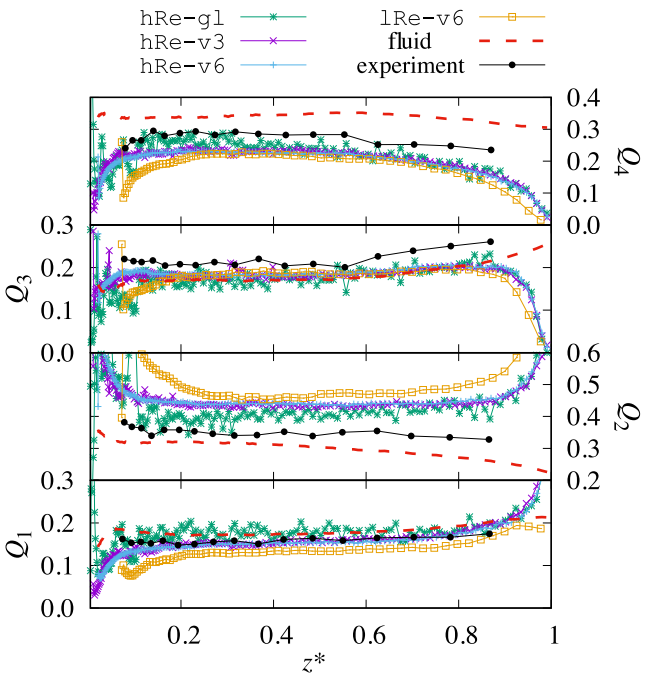

Fig. 21. Fraction of occurrence in each quadrant.

4.5. Quadrant analysis

Fig. 21 shows the fraction of occurrence of each quadrant (Outward interaction Q_1: $u'_f > 0$ and $w'_f > 0$; Ejection Q_2: $u'_f < 0$ and $w'_f > 0$; inward interaction Q_3: $u'_f < 0$ and $w'_f < 0$; sweep Q_4: $u'_f > 0$ and $w'_f < 0$) of the fluid velocity fluctuations at the particle locations. The fraction of occurrence of a quadrant Q_i $(i = 1, 2, 3, 4)$ is defined as:

$$f(Q_i) = \frac{\int_{Q_i} p(u'_f, w'_f)\, du'_f\, dw'_f}{\sum_{j=1}^{4} \int_{Q_j} p(u'_f, w'_f)\, du'_f\, dw'_f}, \tag{24}$$

where $p(u'_f, w'_f)$ is the PDF of the fluid velocity fluctuations. The fraction of occurrence is calculated for each layer $(s = 1, 2, \ldots, N_s)$: using randomly distributed points for the fraction of fluid occurrences, and for the fraction of fluid occurrences at the particle locations using the positions of the particles.

The curves relative to the virtual wall (`hRe-v3` and `hRe-v6`) practically collapse over each other, thus reinforcing the proposition that the position of the virtual wall does not affect in the dynamics of the suspended particles. The case with lift force (`hRe-gl`) shows some oscillations because of the less converged statistics. The curve with virtual wall for $\mathrm{Re}_\tau = 180$ (`lRe-v6`) shows similar results compared to the results with the simulations with $\mathrm{Re}_\tau = 500$; but some deviations are observed which is primarily due to the small channel height in the low Reynolds number. Away from the wall, all simulations show very similar fractions of occurrences.

In the core of the channel (away from the bottom wall), a large proportion of the particles, roughly about 0.45 of the particles are located in the Q_2 event. This is contrasted to the lower fluid occurrences which is just about 0.30. On the other hand, only 0.20 of the particles are located in the Q_4, contrasted to the higher fluid occurrences (about 0.35). These differences of particle and fluid occurrences in the Q_2 and Q_4 events are typical in suspended sediment transport (Breugem, 2012). There are similar particle and fluid occurrences in $Q1$ and $Q3$ events.

From this quadrant analysis, larger fractions of particles in upward fluid motion (Q_1 and Q_2) are observed which are related to the positive

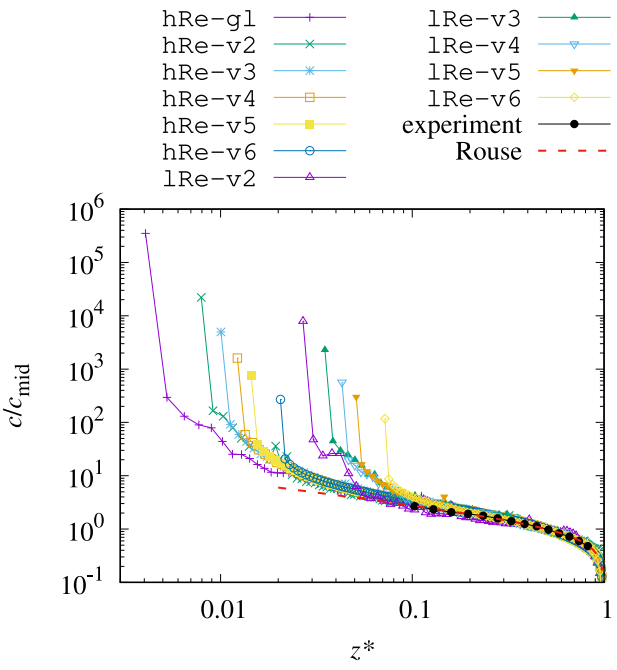

Fig. 22. Particle-concentration profile with closer look in the near-wall region.

vertical drift velocity (Fig. 18), and similarly larger fractions of particles are in Q_2 and Q_3 events associated to the negative streamwise drift velocity. Particularly, the Q_2 event has the larger contribution compared to others events individually. This means that the particles are mostly located in upward fluid motion correlated to the ejection type of events.

4.6. Particle-concentration in the near-wall region

Fig. 22 shows the particle-concentration profiles, similar to Figs. 11 and 14, but now, the x-axis is in logarithmic scale in order to zoom-in the near-wall region. The cases with insufficient suspended particles are excluded. It can be observed that very near the wall, the particle-concentration depends on the position of the virtual wall. However, above a small distance from the wall, all the simulations essentially coincide among themselves, with the experimental results, and with the Rouse profile, as previously observed in above sections. This means that the detailed position of the virtual wall is not important for the motion of suspended sediment, provided that the virtual wall is located in a region where the fluctuations of the wall-normal fluid velocity is similar to the particle settling velocity, or, equivalently, when the virtual wall is located in a region with a local particle Froude number (defined in Eq. (13)) of the order of $\mathcal{O}(1)$. Below $z^* < 0.1$, corresponding to $z^+ < 50$ in wall-unit for $\mathrm{Re}_\tau = 500$ and $z^+ < 20$ in wall-unit for $\mathrm{Re}_\tau = 180$, the simulation results start deviating from the Rouse profile. Actually, the Rouse profile is obtained by assuming a logarithmic mean velocity profile, which is not applicable for z^+ lower than about 50.

For Reynolds number $\mathrm{Re}_\tau = 500$, all results show the same concentration profiles above about $z^* \approx 0.03$, which corresponds to $z^+ \approx 15$ in wall-unit. Also, from Fig. 12 (particle momentum balance for the case with lift force model, `hRe-gl`), it can be observed that from the similar height $z^+ \gtrapprox 15$, the lift force becomes negligible. This means that roughly above the buffer-layer, the dominant forces are gravity and drag, thus, regardless of the way in which the particles are suspended, the simulations including these two forces give the same dynamics of the suspended particles, and the lift force does not play a significant role in these dynamics.

The results presented in this work shows that irrespective of how the particles are re-entrained into suspension, the statistics of particle motion and the relative particle-concentration profiles, above the buffer-layer, are similar each other and agree very well with the experimental results. In this sense, the virtual wall is effective in bringing the particles into suspension, obtaining good results provided the virtual wall is located in a region with local particle Froude number of the order of $\mathcal{O}(1)$. Thus, the virtual wall allows the study of the dynamics of suspended sediment without detail consideration of complex near-wall interactions. This is, regardless the position of the virtual wall affects the near-wall concentration and distribution of the particles, above the buffer-layer, the dynamics is essentially one-way coupling, and thus the point-particle DNS is adequately modelling the suspended sediment transport.

5. Conclusion

In this work, point-particle one-way coupling DNS are performed in order to study the dynamics of the suspended sediment transport in horizontal channel flow. The sediment particles are characterised by the particle-to-fluid density ratio which is slightly larger than one, and the size of the particles which is comparable to the smallest turbulence length-scale. Thus, it is analysed in what extent the point-particle and one-way coupling assumptions are adequate in the modelling of the sediment transport restricted to the motion of suspended sediment, in the absence of the gravitational force, as well as in the presence of this force in wall-normal direction.

In the absence of the gravitational force, the fluid–particle interaction term which contains the fluid acceleration would become important due to the small particle-to-fluid density ratio. The forces associated to the fluid acceleration term are the stress-gradient and the added-mass forces. Particularly, the stress-gradient force becomes dominant, and it balances the turbophoretic effect. The lift force is balanced by the drag force, but these two forces are smaller compared to the stress-gradient and turbophoretic effect. It is observed small velocity lag of particles in streamwise direction, but the relative velocity which drives the drag force is even smaller. Thus, the drag force in streamwise direction can be considered as a secondary effect. The added-mass force is negligible, which is the consequences that the particles are following and adapting to the local fluid-turbulence, *i.e.*, the fluid Reynolds-stresses seen by the particles are very similar to the particle Reynolds-stresses (see the Eqs. (19) and (20)). The particle-concentration profile is nearly uniform; only a slightly larger particle accumulation in the viscous sub-layer is observed, and the turbulent diffusion effect is negligible due to the damping of the turbulence near the wall. All these are contrasted to the applications with gas–solid/liquid flow, where the stress-gradient and added-mass forces are negligible due to the high particle-to-fluid density ratio, and thus the turbophoretic effect is balanced by the concentration-gradient effect with higher particle accumulation in near wall region and by the drag force with higher drifts.

When the gravitational force acts in the wall-normal direction, the particle Froude number becomes a dominant parameter. This means that the particles are accumulated on the bottom wall, and therefore it is necessary to incorporate a resuspension model to take into account the complex resuspension mechanism composed by fluid–particle and inter-particle interactions, which cannot be modelled in the context of one-way coupling simulations. However, away from the wall, the suspended sediment transport is essentially one-way coupled. Thus, a very simple resuspension model which avoid the complex physics in the near wall region is incorporated in the point-particle one-way coupling DNS. This simple resuspension model is a virtual wall consisting of a horizontal plane parallel to the bottom wall and located at a short distance above the bottom wall for the bouncing of the particles. In order to validate the point-particle one-way coupling DNS with the virtual wall for the simulation of the suspended sediment transport, the results of the simulations with the virtual wall are compared to the results of the experiments performed by Breugem (2012). Furthermore, the sensitivity of the position of the virtual wall in the dynamics of

the suspended sediment is analysed based on a local particle Froude number, which is defined as the ratio between the rms of local fluctuating fluid velocity in wall-normal direction to the absolute value of the particle settling velocity (see Eq. (13)).

With the presence of the gravitational force in the wall-normal direction, the lift force is only important in the viscous sub-layer, and above this layer, the lift force is negligible, and the drag force takes account of the gravitational force. The forces associated to the fluid-acceleration term, such as the stress-gradient and the added-mass forces, have an order of magnitude smaller than the gravitational and drag forces in the buffer layer; and in the most part of the channel, these forces are negligible. Similarly, the turbophoretic and the concentration-gradient effects contribute to the particle momentum balances in the buffer layer, but in the rest of the channel, these effects are also negligible. Therefore, above the buffer layer, the drag force and the gravitational force dominate the dynamics of the suspended sediments.

Several statistics of suspended sediment motion are compared to the experimental results, and good agreement are obtained. Furthermore, these results of suspended sediment dynamics from the simulation performed, above the buffer-layer, are insensitive to the position of the virtual wall when this wall was placed in a region where the local particle Froude number is on the order of $\mathcal{O}(1)$. This is despite the near-wall particle distribution and concentration depend on the position of the virtual wall, above the buffer-layer the dynamics becomes insensitive of the virtual wall position. Thus, once the particles are in a region with fluid velocity fluctuation comparable to the particle settling velocity, the drag force is enough to take into account with the gravitational force. Therefore, our results show that the suspended sediment transport can be modelled accurately using the point-particle one-way coupling DNS incorporating the virtual wall as a simple resuspension model; in this sense, the virtual wall can be considered as a wall-function for the motion of particles in the context of the point-particle one-way coupling DNS.

In addition, from the perspective of the development of engineering two-fluid models, our results indicate that the essential mechanism of the suspended sediment transport is determined by the drag and gravitational forces, and the others can be considered as secondary forces.

Declaration of competing interest

The authors declare that they have no known competing financial interests or personal relationships that could have appeared to influence the work reported in this paper.

Acknowledgements

H.H.S. acknowledges the financial supports given by Itaipu Binacional under the Postgraduate Scholarship Program and the short-term scholarship from CONACyT Program 1698/OC-PR. C.E.S. acknowledges FEEI-CONACyT-PRONII. N.M. acknowledges supports from FAPERJ, CNPq, CAPES, and FINEP.

References

Ancey, C., 2020a. Bedload transport: a walk between randomness and determinism. Part 1. The state of the art. J. Hydraul. Res. 58 (1), 1–17. http://dx.doi.org/10.1080/00221686.2019.1702594.

Ancey, C., 2020b. Bedload transport: a walk between randomness and determinism. Part 2. Challenges and prospects. J. Hydraul. Res. 58 (1), 18–33. http://dx.doi.org/10.1080/00221686.2019.1702595.

Arcen, B., Tanière, A., Oesterlé, B., 2006. On the influence of near-wall forces in particle-laden channel flows. Int. J. Multiph. Flow. 32 (12), 1326–1339. http://dx.doi.org/10.1016/j.ijmultiphaseflow.2006.06.009.

Bagnold, R.A., 1966. An approach to the sediment transport problem from general physics. Geol. Surv. Prof. Pap. 422-I, I1–I37. http://dx.doi.org/10.3133/pp422I.

Breugem, W.A., 2012. Transport of suspended particles in turbulent open channel flows (Ph.D. thesis). TU Delft, Delft University of Technology, URL: https://repository.tudelft.nl/islandora/object/uuid:3fa8d72d-c3aa-4786-a321-41433ad1df78?collection=research.

Breugem, W.A., Uijttewaal, W.S., 2006. A PIV/PTV experiment on sediment transport in a horizontal open channel flow. In: Ferreira, R.M.L., Alves, E.C.T.L., Leal, J.G.A.B., Cardoso, A.H. (Eds.), River Flow 2006, Taylor & Francis. In: Proceedings of the International Conference on Fluvial Hydraulics, vol. 1, Lisbon, Portugal, pp. 789–798. http://dx.doi.org/10.1201/9781439833865.

Brownlie, W.R., 1981. Prediction of flow depth and sediment discharge in open channels. W. M. Keck Laboratory of Hydraulics and Water Resources Report 43A, California Institute of Technology, Pasadena, California, http://dx.doi.org/10.7907/Z9KP803R.

Cargnelutti, M.F., Portela, L.M., 2007. Influence of the resuspension on the particle sedimentation in wall-bounded turbulent flows. In: Sommerfeld, M. (Ed.), Proceedings of the 6th. int. conference on multiphase flow. ICMF, Leipzig, Germany, pp. 1–10.

Chanson, H., 2004. the Hydraulics of Open Channel Flow: An Introduction, second ed. Elsevier Butterworth-Heinemann, http://dx.doi.org/10.1016/b978-0-7506-5978-9.x5000-4.

Cherukat, P., McLaughlin, J.B., 1994. The inertial lift on a rigid sphere in a linear shear flow field near a flat wall. J. Fluid Mech. 263, 1–18. http://dx.doi.org/10.1017/S0022112094004015.

Chien, N., Zhaohui, W., 1999. Mechanics of Sediment Transport. ASCE Press, http://dx.doi.org/10.1061/9780784404003.

Coleman, S.E., Nikora, V.I., 2008. A unifying framework for particle entrainment. Water Resour. Res. 44 (4), W04415. http://dx.doi.org/10.1029/2007WR006363.

Dey, S., Ali, S.Z., 2019. Bed sediment entrainment by streamflow: State of the science. Sedimentology 66 (5), 1449–1485. http://dx.doi.org/10.1111/sed.12566.

Drew, D.A., 1983. Mathematical modeling of two-phase flow. Annu. Rev. Fluid Mech. 15, 261–291. http://dx.doi.org/10.1146/annurev.fl.15.010183.001401.

Enwald, H., Peirano, E., Almstedt, A.-E., 1996. EulerIan two-phase flow theory applied to fluidization. Int. J. Multiph. Flow. 22 (SUPPL. 1), 21–66. http://dx.doi.org/10.1016/s0301-9322(96)90004-x.

García, M.H., 2008. Sediment transport and morphodynamics. In: García, M.H. (Ed.), Sedimentation Engineering: Processes, Measurements, Modeling, and Practice. American Society of Civil Engineers Manuals and Reports on Engineering Practice 110, pp. 21–163. http://dx.doi.org/10.1061/9780784408148.ch02.

Kaftori, D., Hetsroni, G., Banerjee, S., 1995. Particle behavior in the turbulent boundary layer. II. Velocity and distribution profiles. Phys. Fluids 7 (5), 1107–1121. http://dx.doi.org/10.1063/1.868552.

Krishnan, G.P., Leighton, D.T., 1995. Inertial lift on a moving sphere in contact with a plane wail in a shear flow. Phys. Fluids 7 (11), 2538–2545. http://dx.doi.org/10.1063/1.868755.

Marchioli, C., Soldati, A., Kuerten, J.G.M., Arcen, B., Tanière, A., Goldensoph, G., Squires, K.D., Cargnelutti, M.F., Portela, L.M., 2008. Statistics of particle dispersion in direct numerical simulations of wall-bounded turbulence: Results of an international collaborative benchmark test. Int. J. Multiph. Flow. 34 (9), 879–893. http://dx.doi.org/10.1016/j.ijmultiphaseflow.2008.01.009.

Maxey, M.R., Riley, J.J., 1983. Equation of motion for a small rigid sphere in a nonuniform flow. Phys. Fluids 26 (4), 883–889. http://dx.doi.org/10.1063/1.864230.

McLaughlin, J.B., 1991. Inertial migration of a small sphere in linear shear flows. J. Fluid Mech. 224, 261–274. http://dx.doi.org/10.1017/S0022112091001751.

McLaughlin, J.B., 1993. The lift on a small sphere in wall-bounded linear shear flows. J. Fluid Mech. 246, 249–265. http://dx.doi.org/10.1017/S0022112093000114.

Monchaux, R., Bourgoin, M., Cartellier, A., 2012. Analyzing preferential concentration and clustering of inertial particles in turbulence. Int. J. Multiph. Flow. 40, 1–18. http://dx.doi.org/10.1016/j.ijmultiphaseflow.2011.12.001.

Muste, M., Yu, K., Fujita, I., Ettema, R., 2009. Two-phase flow insights into open-channel flows with suspended particles of different densities. Environ. Fluid Mech. 9, 161–186. http://dx.doi.org/10.1007/s10652-008-9102-7.

Narayanan, C., Lakehal, D., Botto, L., Soldati, A., 2003. Mechanisms of particle deposition in a fully developed turbulent open channel flow. Phys. Fluids 15 (3), 763–775. http://dx.doi.org/10.1063/1.1545473.

Nezu, I., Azuma, R., 2004. Turbulence characteristics and interaction between particles and fluid in particle-laden open channel flows. J. Hydraul. Eng. 130 (10), 988–1001. http://dx.doi.org/10.1061/(asce)0733-9429(2004)130:10(988).

Niño, Y., Lopez, F., Garcia, M., 2003. Threshold for particle entrainment into suspension. Sedimentology 50 (2), 247–263. http://dx.doi.org/10.1046/j.1365-3091.2003.00551.x.

Portela, L.M., Oliemans, R.V.A., 2003. Eulerian-Lagrangian DNS/LES of particle-turbulence interactions in wall-bounded flows. Internat. J. Numer. Methods Fluids 43 (9), 1045–1065. http://dx.doi.org/10.1002/fld.616.

Portela, L.M., Oliemans, R.V.A., 2006. Possibilities and limitations of computer simulations of industrial turbulent dispersed multiphase flows. Flow, Turbulence and Combustion 77, 381–403. http://dx.doi.org/10.1007/s10494-006-9051-5.

Rashidi, M., Hetsroni, G., Banerjee, S., 1990. Particle-turbulence interaction in a boundary layer. Int. J. Multiph. Flow. 16 (6), 935–949. http://dx.doi.org/10.1016/0301-9322(90)90099-5.

Reeks, M.W., 1983. The transport of discrete particles in inhomogeneous turbulence. J. Aerosol Sci. 14 (6), 729–739. http://dx.doi.org/10.1016/0021-8502(83)90055-1.

van Rijn, L.C., 1984. Sediment transport, part II: Suspended load transport. J. Hydraul. Eng. 110 (11), 1613–1641. http://dx.doi.org/10.1061/(ASCE)0733-9429(1984)110:11(1613).

van Rijn, L.C., 2020. Sand transport. URL: http://www.coastalwiki.org/wiki/Sand_transport.

Rodi, W., 2017. Turbulence modeling and simulation in hydraulics: A historical review. J. Hydraul. Eng. 143 (5), 03117001. http://dx.doi.org/10.1061/(ASCE)HY.1943-7900.0001288.

Rouse, H., 1939. An analysis of sediment transportation in the light of fluid turbulence. Soil Conservation Services Report No. SCS-TP-25, U.S. Department of Agriculture, URL: https://resolver.caltech.edu/CaltechAUTHORS:20140529-132455484.

Shields, A., 1936. Anwendung der Aehnlichkeitsmechanik und der Turbulenzforschung auf die Geschiebebewegung. [English title: Application of similarity principles and turbulence research to bed-load movement / by Ing. A. Shields; translated by W.P. Ott and J.C. van Uchelen]. W. M. Keck Laboratory of Hydraulics and Water Resources, Hydrodynamics Laboratory, Technical Report 167, California Institute of Technology, Pasadena, California, URL: https://resolver.caltech.edu/CaltechKHR:HydroLabpub167.

Simonin, O., Deutsch, E., Minier, J.P., 1993. Eulerian Prediction of the fluid/particle correlated motion in turbulent two-phase flows. Appl. Sci. Res. 51, 275–283. http://dx.doi.org/10.1007/BF01082549.

Soldati, A., Marchioli, C., 2012. Sediment transport in steady turbulent boundary layers: Potentials, limitations, and perspectives for Lagrangian tracking in DNS and LES. Adv. Water Resour. 48, 18–30. http://dx.doi.org/10.1016/j.advwatres.2012.05.011.

Sotiropoulos, F., 2015. Hydraulics in the era of exponentially growing computing power. J. Hydraul. Res. 53 (5), 547–560. http://dx.doi.org/10.1080/00221686.2015.1119210.

Sotiropoulos, F., 2019. Hydraulic engineering in the era of big data and extreme computing: Can computers simulate river turbulence? J. Hydraul. Eng. 145 (6), 02519002. http://dx.doi.org/10.1061/(ASCE)HY.1943-7900.0001594.

Vinkovic, I., Doppler, D., Lelouvetel, J., Buffat, M., 2011. Direct numerical simulation of particle interaction with ejections in turbulent channel flows. Int. J. Multiph. Flow. 37 (2), 187–197. http://dx.doi.org/10.1016/j.ijmultiphaseflow.2010.09.008.

Vollmer, S., Kleinhans, M.G., 2007. Predicting incipient motion, including the effect of turbulent pressure fluctuations in the bed. Water Resour. Res. 43 (5), W05410. http://dx.doi.org/10.1029/2006WR004919.

Wang, Q., Squires, K.D., Chen, M., McLaughlin, J.B., 1997. On the role of the lift force in turbulence simulations of particle deposition. Int. J. Multiph. Flow. 23 (4), 749–763. http://dx.doi.org/10.1016/S0301-9322(97)00014-1.

Wu, W., 2007. Computational River Dynamics. CRC Press, http://dx.doi.org/10.4324/9780203938485.

Zeng, L., Balachandar, S., Fischer, P., Najjar, F., 2008. Interactions of a stationary finite-sized particle with wall turbulence. J. Fluid Mech. 594, 271–305. http://dx.doi.org/10.1017/S0022112007009056.

Zeng, L., Najjar, F., Balachandar, S., Fischer, P., 2009. Forces on a finite-sized particle located close to a wall in a linear shear flow. Phys. Fluids 21 (3), 033302. http://dx.doi.org/10.1063/1.3082232.